Carbon 178 (2021) 391–412

Contents lists available at ScienceDirect

Carbon

journal homepage: www.elsevier.com/locate/carbon

Review article

Interfacial heat transport in nano-carbon assemblies

Lin Qiu [a], Xiaohua Zhang [b, *], Zhixin Guo [c], Qingwen Li [d]

[a] School of Energy and Environmental Engineering, University of Science and Technology Beijing, Beijing, 100083, China
[b] Innovation Center for Textile Science and Technology, Donghua University, Shanghai, 201620, China
[c] State Key Laboratory for Mechanical Behavior of Materials, Xi'an Jiaotong University, Xi'an, 710049, China
[d] Division of Advanced Nano-Materials, Suzhou Institute of Nano-Tech and Nano-Bionics, Chinese Academy of Sciences, Suzhou, 215123, China

ARTICLE INFO

Article history:
Received 23 November 2020
Received in revised form
23 February 2021
Accepted 25 February 2021
Available online 22 March 2021

Keywords:
Nano-carbon assembly
Interfacial heat transport
Thermal conductivity
Low-frequency phonons
Measurement methods

ABSTRACT

Although the individual one- and two-dimensional (1D and 2D) carbon nanostructures possess extremely high thermal conductivity, their macroscopic assemblies do not efficiently utilize it due to the larger interfacial contact thermal resistance. To improve the overall performance, the key is the interfacial structure design to provide sufficient pathways for phonon transport with a limited sacrifice or damage to the inherent thermal properties of nanomaterials. Particularly, the resonance of low-frequency lattice vibrations is the most important mechanism for the reduction of the interfacial contact thermal resistance. Based on recent theoretical and experimental studies and observations on interfacial heat transport, we review here a fourfold set of transport problems in this field: (1) low-frequency phonons in 1D and 2D nanostructures for heat transport; (2) the mechanisms of interfacial thermal transport; (3) assembly structure design towards high utilization of the thermal conductivity from individual nanostructures; and (4) recent development of thermal conductivity measurement for individual and assembled nanomaterials.

Contents

* Corresponding author.
E-mail address: zhangxh@dhu.edu.cn (X. Zhang).

https://doi.org/10.1016/j.carbon.2021.02.105
0008-6223/

1. Introduction

With relentlessly decreasing sizes of devices and structures, the thermal transport becomes more and more severe, pushing the rapid development of thermal interface materials (TIMs). Nano-carbon materials, including carbon nanofibers (CNFs), carbon nanotubes (CNTs), graphene sheets, and graphene nanoribbons (GNRs), have shown a strong potential for the application as TIMs due to their inherent high thermal conductivity [1–6]. Unfortunately, although nano-carbons possess a high conductivity, on the order of 10^2–10^3 W m^{-1} K^{-1}, the effective conductivity of the TIMs using them as fillers is only on the order of 1–10 W m^{-1} K^{-1}. A better strategy to use nano-carbons is to assemble them into a large-size material, like fibers and films, whereas the heat conduction across the interface between nano-carbons has become a key factor limiting the overall thermal properties. To understand the mechanism of heat transport in nano-carbon assemblies, and thus to develop the enhancement strategies, it is necessary to investigate thermal energy transport at interfaces. Therefore, various problems including the physics of phonon transport in nano-carbons, the interfacial heat transport, the assembly structure design and optimization, and experimental measurement strategies, should be investigated with great effort and carefulness.

First of all, for individual nano-carbons, there are new physics and novel thermal properties different from bulk materials, such as the abnormal heat conduction, size dependence of thermal conductivity, and phonon boundary/edge scatterings [7,8]. For bulk materials, heat conduction has been long time considered as a diffusion process governed by Fourier's law,

$$J = -\kappa \nabla T, \tag{1}$$

where J is the local heat flux, ∇T the temperature gradient, and κ the thermal conductivity which should be size independent. However, this law fails in one-dimensional (1D) lattices as size dependence raises up. For example, for a Fermi-Pasta-Ulam (FPU) chain with a simple anharmonic approximation to the Hamiltonian, e.g., $H = \sum_i \frac{p_i^2}{2} + \frac{1}{2}(x_i - x_{i-1})^2 + \frac{\beta}{4}(x_i - x_{i-1})^4$, κ diverges with the lattice length L approximately as $L^{1/2}$ [9]. It is found that the phonon–lattice interaction is the key factor for Fourier's law [10]. For nano-carbons in which such interaction is not significant, theoretical and experimental results have also confirmed the similar length-dependent divergence of κ [4,11–13]. Furthermore, κ does not converge even if its length is much larger than the phonon mean free path [7]. These discoveries are consistent with the investigations on the atomic-chain model, that is, only the phonon–phonon interaction cannot give rise to Fourier's law. Consequently, in nano-carbons such as CNT, graphene, and GNR, the conductivity is mostly ascribed to low-frequency phonons (LFPs), owing to their high phonon velocities and/or large mean free paths [14–20].

When nano-carbons are assembled together, interfaces appear and the contact thermal resistance becomes the key problem for thermal transport. For example, when CNTs are bundled together the conductivity along the bundle axis is just one third that of an individual CNT, and in the perpendicular direction it is even two orders of magnitude smaller [21]. The across-tube thermal resistance between CNTs is found to be strongly influenced by the contact type (crossed or parallel), and the pressure applied on them as well [22]. Similarly, the resistance between graphene sheets also determines the conductivity of graphene assemblies [23–27]. Thus the contact engineering for nano-carbons is very important, and the mechanism of interfacial thermal transport should be clarified in advance. Here the situation is limited to a small group of nano-carbons.

When massive nano-carbons are assembled into macroscopic materials, there are more factors affecting the thermal conductivity, such as the packing density, orientation, and flaws in assembly structure [28]. Thus far, although it is still a challenge to produce high-quality assemblies of nano-carbons, various important achievements have been realized. Therefore, it is necessary to establish the structure–property relationship for nano-carbon assemblies at the macroscopic scale.

Moreover, as the dimensions, density, and surface morphology of these nano-carbon assemblies are greatly different from the conventional large-size materials, it is also a challenge to precisely measure their thermal properties. There have existed more than ten types of measurement methods successfully applied to various nano-carbon materials, while each has its own limitation. Based on the special assembly feature of nano-carbons, it is also necessary to remedy the existing measurement methods.

In this paper, we start with a section to introduce the fail of Fourier's law in low-dimensional systems, and thus lead to the concept of LFPs which play an important role in determining the capacity of heat transport for nano-carbons. Consequently, we also discuss in this section the influences of interfacial phonon coupling on the heat transports in and between nano-carbons, including the theoretical modelling as well. In the next section, the thermal conductivity of macroscopic nano-carbon assemblies is reviewed according to the dimensionality, to show the effect of various assembly forms. This section is organized into experimental progresses, strategies to improve thermal performances, and recent theoretical investigations. Subsequently, considering the various dimensionality and assembly structure, the measurement techniques for accurate evaluation of thermal conduction are summarized and discussed in a new section, by focusing on the applicability and possible development toward nano-carbon assemblies. The above scheme is schematically depicted in Fig. 1. Finally, we draw a conclusion and provide future directions for this research field.

2. Low-frequency phonons in nano-carbons

2.1. Ballistic and diffusive phonon transports

In the past dozen years, the thermal conductivity of low-dimensional nano-carbon materials, such as CNT, GNR, and graphene, have attracted great attentions owing to their novel thermal transport properties. Similar to the investigation on 1D lattice models [9,10], the divergent κ was also observed in nano-carbons. Non-equilibrium molecular dynamics (NEMD) simulations revealed that the conductivity of a CNT diverges as $\kappa \propto L^{\alpha}$, where L is the tube length and $\alpha = 0.27$, 0.15, and 0.11 for the (5,5), (8,8), and (10,10) CNTs at 300 K (Fig. 2A) [29]. (Larger α values were also

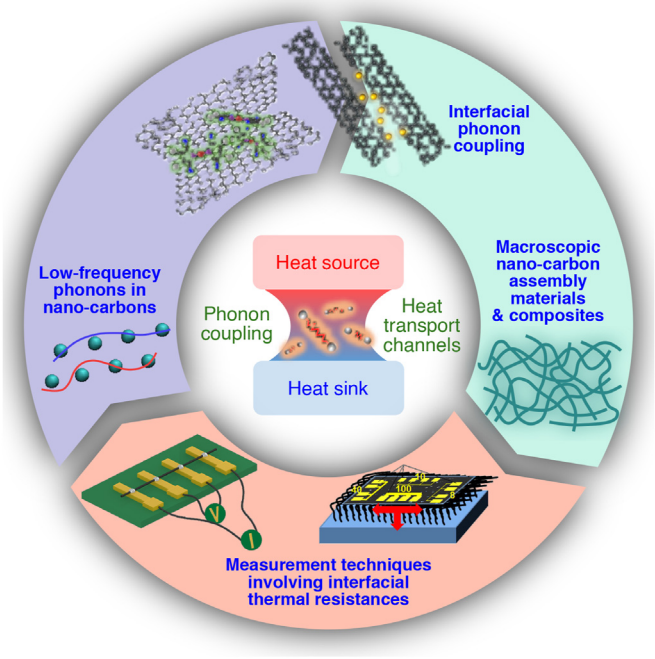

Fig. 1. Scheme of interfacial heat transport in nano-carbon assemblies. (A colour version of this figure can be viewed online.)

reported, e.g., 0.4 and 0.36 for the (5,5) and (10,10) CNTs at 300 K [12]). Here, a larger α value is attributed to the smaller CNT length, where a more ballistic phonon transport is expected [30]. The similar power law was also observed in GNRs; $\alpha = 0.47$ and 0.35 for 2-nm-wide armchair and zigzag GNRs, respectively (Fig. 2B) [4]. Due to the scattering of different edge-localized phonons, there is also a large anisotropy in thermal conductivity for GNRs, which can be controlled by the GNR width, edge roughness, and hydrogen termination, as the edge–phonon scattering plays a negative effect on the conductivity [31].

There is competition between the ballisticity of phonon transport and phonon scattering, as reflected by using such simple formula of $\kappa \propto L^{\alpha}$, where α is expected to decrease when L increases from a ballistic size to a diffusive phonon-transport size. This is because the anharmonicity of nanomaterials can be enhanced with increasing the size, due to the strengthened phonon scattering. For example, the conductivity of (5,5) CNT shows a linear dependence with L ($\kappa \propto L$) when $L < 40$ nm and a power law ($\kappa \propto L^{\alpha}$) otherwise [32]. ($\alpha \approx 0.62$ when $40 < L < 200$ nm and $\alpha \approx 0.26$ when $200 < L <$ 3000 nm.) Further increasing L up to >10 μm, the thermal conduction becomes very close to the completely diffusive transport, and the ballistic transport can be ignored [30]. Thus far, it is known that LFPs possess long phonon mean free paths, and lattice defects can scatter the LFPs more efficiently and reduce significantly their contribution to the thermal transport.

To provide a more realistic description, an empirical formula $\kappa = \kappa_{\infty}(1 - e^{-L/L_c})$ was proposed, where κ_{∞} is the fit fully diffusive thermal conductivity and L_c a fit length to describe the transition from ballistic to diffusive phonon transport [33]. It can be roughly considered that, the ballistic phonon transport dominates the thermal conductivity, when L is smaller than L_c and the phonon mean free path is limited to L owing to the boundary scatterings, resulting $\kappa \propto L$. Whereas, when L is much larger than L_c, the diffusive phonon transport dominates, and the mean free path is limited by the phonon scatterings, resulting in the L-independent κ. Therefore, when L is comparable to L_c, the phonon mean free path is determined by the combined contribution of boundary and phonon scatterings.

The similar divergence of Fourier's law was also observed in 2D nano-carbons, but with a different size dependence, i.e., $\kappa \propto \log L$ [34–36]. This logarithmic dependence was experimentally and theoretically verified in single-layer graphene, see Fig. 2C and D [13]. Experiments showed that κ does not saturate even in a superlong sample with $L \approx 8$ μm, because the logarithmic dependence arises for $700 < L < 9000$ nm (Fig. 2C), as confirmed by NEMD simulations in the regime of $5 < L < 1000$ nm (Fig. 2D). Similar to the 1D case, the divergence of κ out of the usual ballistic region is attributed to the reduced dimensionality, while the different size dependence indicates that the LFPs are quite different in the 1D and 2D nano-carbons [37,38].

2.2. Low-frequency phonons

It has been clear that LFPs, especially the acoustic ones, have very long mean free paths in 1D nano-carbons such as CNTs and GNRs, and are mainly responsible for the unusually high thermal conductivity and the intriguing length divergences [14,16–19,30,39–41]. In such 1D materials, there are four acoustic modes: longitudinal acoustic (LA), twisting acoustic (TWA) and doubly degenerate transverse acoustic (TA) [42]. Similarly, for 2D nano-carbons, LFPs are also of great importance. (Fig. 3A shows the phonon dispersions in few-layer graphenes with the Bernal (AB) stacking [41].) The phonon branches along the ΓA direction are acoustic (A) and optical (O) with an in-phase and counterphase movement of the adjacent layers, respectively. These modes can be longitudinal (L) or transverse (T) for the atomic displacements along or perpendicular to the wave vector, respectively. The LFP branches along the ΓK direction can be classified similarly, and the only difference is in the transverse branches, which are denoted by T and Z for the in-plane and out-of-plane atomic displacements, respectively. (The acronyms for the branches along the ΓA direction are primed.)

As an important feature for a phonon, its mean free path, as defined by the average distance traveled by the phonon between successive collisions, is a function of the phonon frequency. The LFPs have a larger mean free path than the others. For example, the effective room temperature mean free path in CNTs can exceed 10 μm for sub-0.5-THz LFPs and is just 10–100 nm for over-20-THz high-frequency phonons (HFPs) [48]. As the main source of thermal resistance is from the collisions between phonons, the larger mean free path of LFPs leads to longer energy transfer distance, less scattering and more efficient heat transfer. Meanwhile, the proportion of HFPs is very small, while the LFPs have an absolute advantage in the density of states (DOS); and the relaxation time of LFPs is also generally longer. Clearly, the contribution of LFPs to heat conduction is dominant. Besides this, the finite size of nano-carbons constrains the phonon motion and causes the thermal conductance to appear size dependence. For example, MD simulations showed that there are more and stronger LFPs in longer CNTs (Fig. 3B), leading to the divergence of thermal conductivity [45]. Furthermore, in terms of phonon scattering, the LFPs mainly scatter through the three-phonon process (a type of phonon coupling), while the HFPs are more scattered by interface disorders, causing their heat-carrying capacity to decrease [49].

For graphenes, there is a strong effect of inter-layer stacking on the LFPs. Fig. 3C shows the phonon DOS of single-layer and bilayer graphenes, calculated using the phonon dispersions in the framework of lattice dynamics theory [46,50]. The peaks at 452, 605, and 638 cm^{-1} correspond to the ZA, TA, and ZO (out-of-plane optic) phonon branches at edge of Brillouin zone, the peak at 1192 cm^{-1} is associated with the low-velocity LA phonons from different directions near the edge of Brillouin zone, the peak at 889 cm^{-1} is

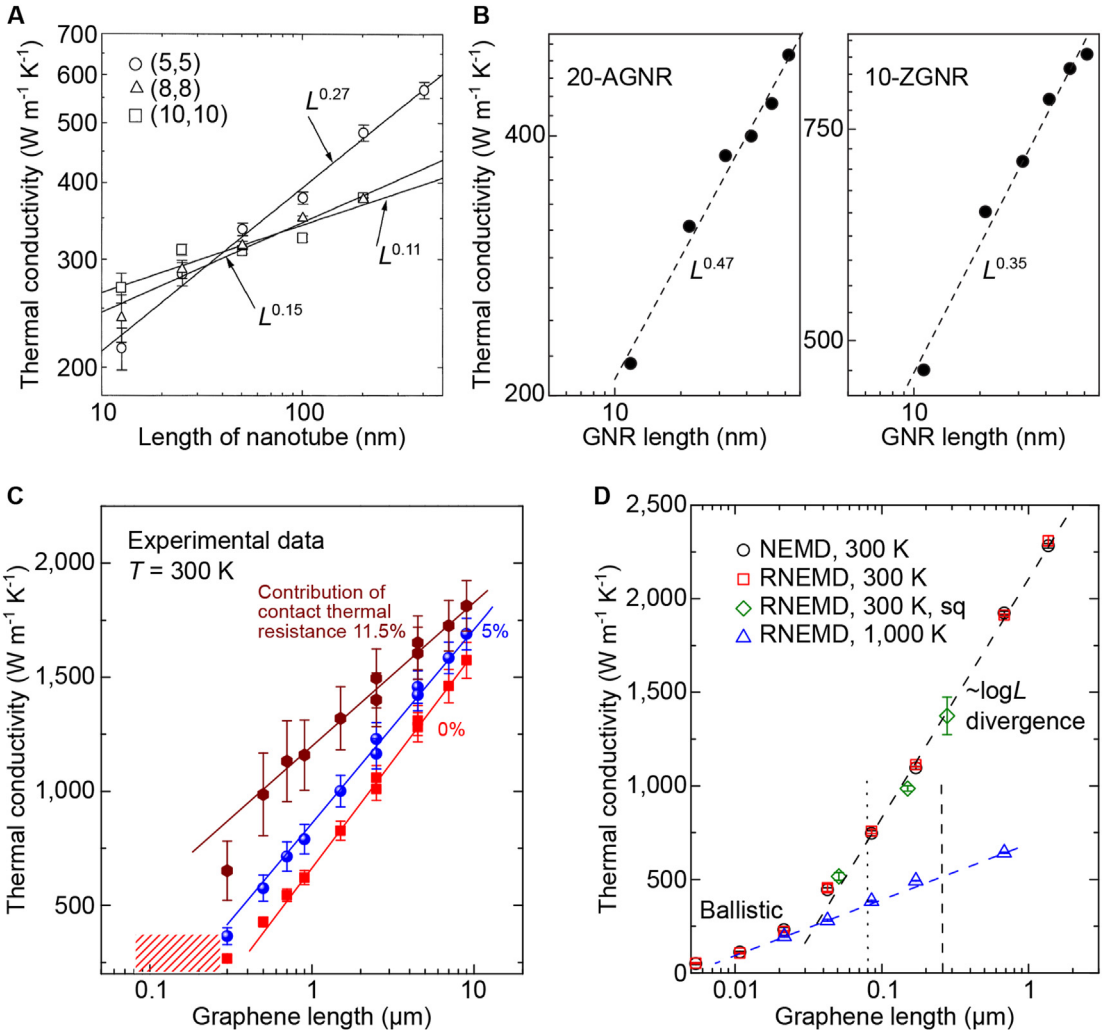

Fig. 2. Length-dependent thermal conductivity for the 1D and 2D nano-carbon materials. (A) For (5,5), (8,8), and (10,10) CNTs at 300 K, $\alpha = 0.27$, 0.15, and 0.11, respectively [29]. (B) For the 20-AGNR and 10-ZGNR (both about 2 nm in width), $\alpha = 0.47$ and 0.35 at 300 K [4]. (C) Length dependence for suspended single-layer graphenes [13], by assuming that the contact thermal resistance is negligible (red squares), 5% (blue circles) and 11.5% (brown diamonds) to the total measured resistance in a 9-mm-long sample. The red diagonal lines indicate the range of phonon mean free path. (D) Thermal conductivity of graphene as a function of the distance between the hot and the cold reservoirs [13], obtained with direct (black circles) and reverse NEMD (red squares and green diamonds) at $T = 300$ K and reverse NEMD at 1000 K (blue triangles). Results obtained with supercells with square aspect ratio (green diamonds) agree well with those obtained with elongated supercells (all others). The dotted and dashed vertical lines indicate the limit of the ballistic transport regime obtained by experiment and simulation, respectively. (A colour version of this figure can be viewed online.)

related to ZO phonon at Γ point, and TO and LO phonons at the center and edge of Brillouin zone are responsible for peaks at 1350 and 1585 cm^{-1}. For the bilayer graphene, the stacking increases the intensity of phonon DOS by a factor of ~2, and generates new phonon modes from the inter-layer interaction. As shown in Fig. 3C, a new DOS peak related to ZA_2 phonons at Γ point appears at 91 cm^{-1}, which is considered as the bilayer analogs of the ZA polarizations of single-layer graphene and can be tuned by the twist angle between graphene layers [50]. It means that the coupling between graphene layers can affect both the in-plane and cross-plane heat transport. New breathing modes were also observed in disorderly stacked few-layer graphenes at 120 and 180 cm^{-1}, namely a combination mode (E_g + ZO′) of the in-plane shear and the inter-layer optical breathing modes and an overtone mode (2ZO'), respectively [51].

To increase the DOS intensity of LFPs, attentions are paid to the effects of temperature, defects, and surface functionalization, besides increasing the size of nano-carbons [52]. For CNTs, a continuous theory was developed to describe the LFP dynamics and related low-temperature physics of axially stressed CNTs [53]. It is found that a tensile stress increases the CNT's eigen frequencies, especially for the modes with radial polarization, while an axial compression decreases them. Such effect is originated from the stress-induced change in graphene's modulus [54,55]. The major influences of CNT chirality, diameter, and orientation of Stone–Wales defects on the DOS are found in the low-frequency regime [56]. For example, vacancy defects and curvature have a strong effect on the Raman-active E_{2g} mode, whose frequency decreases with increasing the defect density and curvature [57]. The defects and curvature also induce a phenomenon of phonon localization, where some sharp peaks appear in the low-frequency region and some high-frequency peaks vanish. Overall, the introduction of defects is a negative effect to suspend the density of LFPs due to the increased possibility of phonon scattering. The effect of defects is also strong for 2D nano-carbons. As shown in Fig. 3D, at high defect concentrations, new DOS peaks appear at the low-frequency regime of bilayer GNRs, especially for the ZA_2 out-of-plane acoustic phonon at ~100 cm^{-1} [47]. By properly folding

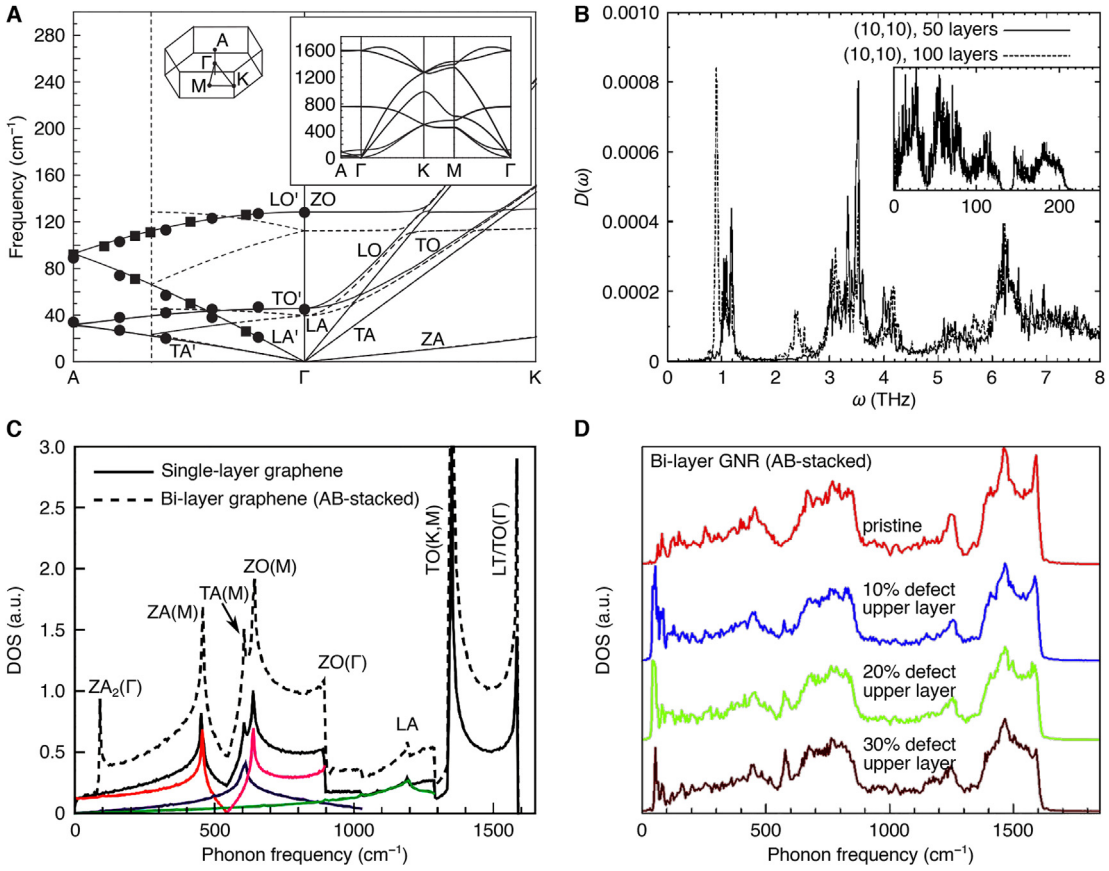

Fig. 3. Low-frequency phonons in nano-carbons. (A) Low-frequency phonon dispersion of Bernal graphite along two high-symmetry directions [41], in comparison with available experimental data, shown by circles [43] and squares [44]. The dashed lines are the dispersion of rhombohedral graphite and the vertical dashed line is the Brillouin zone boundary. Left inset: Brillouin zone of graphite with selected special points. Right inset: Phonon dispersion of Bernal graphite along high-symmetry directions. (B) Vibrational DOS of (10,10) CNT with 50 and 100 layers, respectively [45]. The inset shows the DOS in the full frequency range, and the full graph shows the DOS in the low-frequency range. (C) Phonon DOS of single-layer and AB-stacked bilayer graphene [46]. The contribution from ZA (red), TA (blue), ZO (magenta) and LA (green) phonon branches are also plotted. (D) Phonon DOS of bilayer GNR (ribbon width 2.6 nm) at different concentrations of vacancy defect in the upper layer [47]. (A colour version of this figure can be viewed online.)

few-layer graphenes, the ultra-low frequency inter-layer shear mode can be effectively enhanced, and the van Hove singularity caused by folding can also significantly enhance such shear mode [58].

2.3. Interfacial phonon coupling

2.3.1. Theoretical description

In real applications, nano-carbons are always assembled together to construct rich contacts between them. Hence, understanding the contact thermal resistance is of primary significance to design advanced TIMs. There are several theoretical approaches to describe the phonon transport/coupling across interfaces, such as MD simulation, atomistic Green's function method, and phonon Boltzmann equation modeling [59,60]. The former two are more suitable for small and simple structures due to the large consumption of computational resources, and the latter provides a robust and feasible tool with a clear physical picture of phonon scattering. Thus far, there are mainly two classical models for interfacial phonon transmission based on phonon Boltzmann equation, e.g., the acoustic mismatch model (AMM) [61] and the diffuse mismatch model (DMM) [62]. The AMM assumes that the phonon completely specularly transmits or reflects as acoustic waves at the interface. It was subsequently improved by including the anharmonic atomic vibration at the interface. However, this model has obvious limitations, because it assumes that the interface is ideally smooth, leading to the specular reflection assumption. On the contrary, the DMM proposed assumes that the interface is completely disordered, and the phonon diffuses elastically and loses memory of its incident wave vector and polarization when arriving at the interface. The DMM can be used to establish an upper bound for the across-interface heat transport, as limited by the phonon DOS [63]. In both models, a crucial factor determining the interfacial thermal resistance is the overlap of phonon states. Both models can predict the thermal resistance at low temperatures very well, while at high temperatures most of the practical interfaces are not consistent with the corresponding assumptions, leading to great discrepancy for the results between the model predictions and experiments.

Therefore, based on the AMM and DMM models, the upper and lower bounds of interfacial thermal conductance are determined, and thus can be used to assist the analysis of MD simulations. However, these models could be problematic as they only take into account the elastic phonon scattering and ignore the contribution of the inelastic scattering, leading to the underestimation as compared to experiments [64]. It has been proved that the contribution of inelastic scattering can be over 50% even at room temperature to the total thermal conductivity for interfaces with large acoustic mismatch [65]. When the mass difference between the two materials is large, the surface inelastic transport can involve four- and five-phonon processes and the optical phonon modes can contribute comparable thermal conductance as the acoustic modes

[66]. By developing an effective Debye DOS of phonons and considering the inelastic scattering processes, it has been proved that the vibrational mismatch can provide additional thermal transport channels, especially at high temperatures [67]. As compared to the classical DMM model, such modified DMM model can give a 10-fold increase in thermal conductance, in better agreement with the experimental results [68]. For the Au/graphene interface, such DMM model shows a boundary conductance of 22.8 MW m^{-2} K^{-1} at 300 K (experimental result 21–26 MW m^{-2} K^{-1}), among which the two-, three-, and four-phonon processes contribute 13.3, 6.5, and 2.9 MW m^{-2} K^{-1} to the total conductance, respectively.

Moreover, to consider the interface roughness, a mixed mismatch model (MMM) was proposed, in which the ratio of the specular and diffuse transmissions is determined by the interface and also related to the DOS of phonons [69]. The model is suitable for the prediction of interfacial resistance with arbitrary roughness for carbon-based TIMs. The resistance increases with the surface roughness, and such effect is more significant at low pressures.

Furthermore, for the nano-carbon/metal interfaces, the interfacial thermal transport can also be affected by the coupling between the electrons in metal and the phonons in nano-carbons, which is beyond the scope of the above models. Therefore, new strategies should be introduced into the AMM/DMM models, or combined with MD simulations. For example, by using the result of a density functional theory (DFT) calculation predicting the electron–phonon coupling of noble metals, it is found that such coupling can enhance the apparent thermal interface conductance of the acoustic mismatched interface even by two orders of magnitude [70]. In another approach, based on NEMD simulation and Green's function method combined with DFT, the electron-mediated heat transfer was calculated [71]. The results show that the electron–phonon coupling in CNT/Cu can provide an equivalent contribution to the overall interfacial thermal conductance as compared to that of phonon-based heat transfer.

Clearly, although the AMM and DMM models can improve the understanding of interfacial heat transport, the accuracy of these models is restricted by the rough assumption of phonon scattering, e.g., lack of high-order scattering processes and electro–phonon coupling. As the transmission coefficient calculated by DMM is about two orders of magnitude lower than that calculated by AMM, these models calculate the upper and lower limits of interfacial resistance spanning over a super wide range. Therefore, it is necessary to establish more accurate description of interfacial phonon scattering or transmission into these models, based on the MD and *ab initio* investigations. For example, MD simulations at the atomic level is very helpful to understand the thermal transport of nano-carbons, especially the phenomenon taking place at the interfaces between nano-carbons and substrates. Thus in the following discussions, various MD simulations are introduced in separate topics.

2.3.2. In-plane heat transport

For the contacted nano-carbons, the interfacial phonon coupling becomes a key problem for heat transfer, either across the interface or along (parallel) the nano-carbon itself. For the parallel transport, multi-layer graphenes or GNRs are a typical example to investigate the effect of interfacial interaction. Generally speaking, the in-plane phonon modes (LA and TA) dominate the in-plane heat transport, while the out-of-plane modes (ZA) determine the cross-plane or interfacial heat transport via the phonon coupling. It is found that the thermal conductivity rapidly reduces from ~ 4000 W m^{-1} K^{-1} for a single-layer graphene to ~2800–1300 W m^{-1} K^{-1} when the number of graphene layer reaches 2–4 [17]. Such change is ascribed to the cross-plane coupling of LFPs and the Umklapp scattering for the LA and TA phonons. For the thermal transport in multi-layer graphene, the ZA phonons have a very dominating contribution via the normal phonon scattering [19]. Therefore, based on the investigation of the possible three-phonon scattering events, it is found that the effect of inter-plane interactions can open many new pathways for phonon scattering, most notably for those involving three ZA phonons [72]. Similarly, for the phonon DOS of multi-layer GNRs, the coupling can induce remarkable shrinkage and weakening for the LFPs within 1200–1600 cm^{-1} at the edge of nanoribbons, and the cross-plane coupling can take place mainly for the LFPs within 300–600 cm^{-1}, see Fig. 4A [73]. As a result, the in-plane heat transport is suppressed by the cross-plane coupling.

The interfacial coupling also results in remarkable decrease in thermal conductivity for other nano-carbons. For example, the conductivity of GNRs rapidly decreases with the thickness increasing from monolayer to bilayer, and the reduction is up to 67% when the number of layer reaches 4 [74]. Considering the important contribution of ZA phonon coupling, by artificially freezing the out-of-plane atomic vibration in one layer, the conductivity along such layer would increase from 334 to 467 W m^{-1} K^{-1}, while the conductivity along the other layer is nearly unaffected. When the freezing is on both layers, the bilayer GNR shows the same conductivity as a monolayer GNR.

The presence of a substrate has also a strong and negative influence on the in-plane heat transport for nano-carbons. For a multi-layer graphene supported on an amorphous substrate, the in-plane conductivity is strongly suppressed, and the thickness of multi-layer graphene needs to be more than 30 layers to recover the graphite's conductivity [76]. This is because that the phonon scattering at the interface, as influenced by interface roughness, results in a reduction of the basal-plane phonon mean free path. Similarly, for a GNR/SiC contact, the SiC substrate also significantly reduces the GNR's conductivity by the strong interfacial interaction. Interestingly, when a bilayer GNR is supported on SiC, one GNR layer acts as a buffer layer, and the other GNR layer shows the highest thermal conductivity. There is also an effect from the GNR edge. When the graphene-substrate interaction is weak, the defect has a strong influence on the strengthening of interfacial coupling, while for a strong graphene-substrate interaction, the effect of defect is not large.

Note that there could be about 80% reduction in thermal conductivity for a single-layer graphene when being supported on amorphous SiO_2 (down to ~600 W m^{-1} K^{-1} at room temperature), because of the leaking of phonons across the interface and the strong scattering of ZA phonons [20]. Based on MD simulations, it is found that there is an order-of-magnitude reduction in thermal conductivity due to the damping of ZA modes [77]. However, such suppression can be modulated by the substrate coupling, or in terms of the graphene-substrate interaction. For a strong interaction, the ZA modes can hybridize with the SiO_2 Rayleigh waves, leading to a linearized dispersion relation, higher group velocity, and enhanced thermal transport. This is quite similar to the case of double Frenkel–Kontorova chains, where the inter-chain interaction always enhance rather than suppress the thermal conductance [78].

In several investigations, it is indeed observed that the substrate can also increase the conductivity for nanostructures. With a model containing two coupled FPU chains (Fig. 4B, top panel), a competitive mechanism on the variation of thermal conductivity is obtained [75]: i) phonon scattering due to the interfacial phonon resonance decreases the conductivity (negative effect), and ii) the reduction of intrinsic scatterings between phonons increases the conductivity (positive effect). To describe the inter-chain coupling, a parameter of resonance angle $\Psi = |\arctan(\lambda_2/\lambda_1)|$ is used, where $\lambda_{1/2}$ are the phonon amplitudes of the two FUP chains, and is

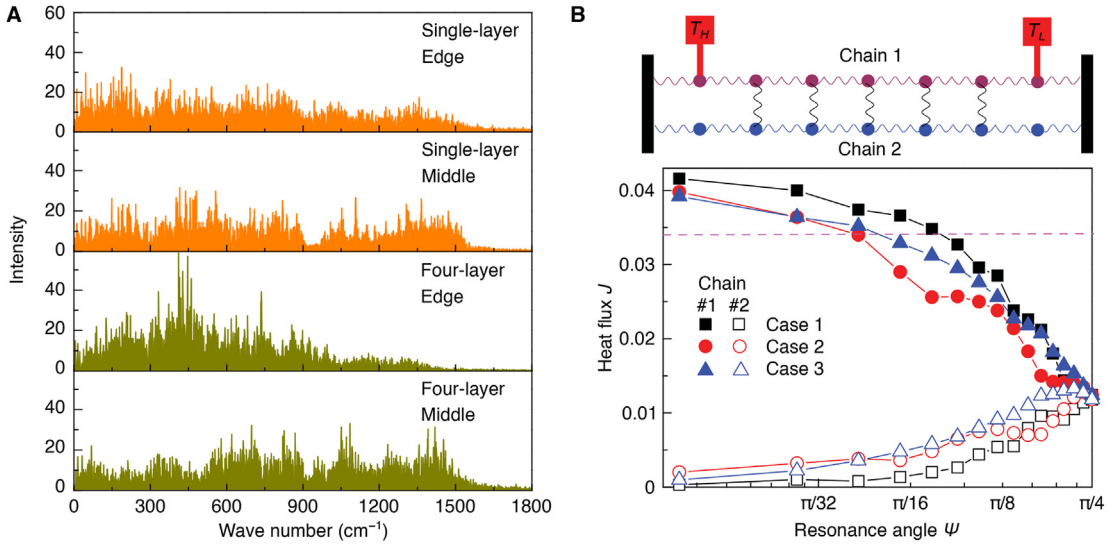

Fig. 4. Effect of interface on the in-plane heat transport of graphene. (A) Spatially resolved phonon spectrum in zigzag graphene with single and four layers, respectively [73]. (B) Schematic of two coupled FPU chains (top panel) and the calculated heat flux J along the two chains as a function of resonance angle Ψ (bottom panel) [75]. The dashed line indicates the heat flux of isolated chain 1. The three cases correspond to different groups of atomic atom and spring constant for the coupled chains, details see Ref. [75]. (A colour version of this figure can be viewed online.)

determined by the atomic mass and spring constant of the coupled chains. When Ψ is small ($<\pi/24$), the variation of thermal conductivity is dominated by the positive effect, while the negative effect dominates when $\Psi > \pi/12$ (Fig. 4B, bottom panel). According to this mechanism, the positive effect was realized in a modified double-wall CNT and an ice-nanotubes coupled within a CNT [75,79], where the vdW interaction from the outer-tube increases the tangential elastic modulus (the out-of-plane force constants) of the inner-tube. As a result, the frequency of ZA phonon in the low-frequency region upshifts, and thus reduces the intrinsic phonon scatterings at room temperature as less phonons are excited. Thus, it is expected that it might be possible to increase the conductivity of 2D nano-carbon via an appropriate coupling between the substrate.

2.3.3. *Cross-plane heat transport*

The interfacial phonon coupling has more important effects on the cross-plane (interfacial) heat transport, which is still a very hot topic thus far. When the heat is transferring, there is usually an obvious temperature jump across the interface, based on which one can define the interfacial thermal resistance [62,80]. A large number of investigations have been performed to understand such interfacial resistance, to show the effect of chemical bonding and vdW interactions [81–89], and various studies also shown that the coupling of LFPs is particularly important for the cross-plane heat transport. Furthermore, the interfacial thermal conductance between nano-carbon and other materials is also of great importance, such as CNT/Si [82,90], CNT/SiO_2 [91], CNT/Cu [71], graphene/silicene monolayer [84], graphene/Cu [92], graphene/water [93], and so on. Taking the heat transport between CNTs as an example, it is mainly constrained by the following two problems: the energy contained in HFP modes should first be transferred to LFP modes via phonon coupling, and efficient pathways should be established to exchange the energy with the LFPs.

The way in which nano-carbons are connected determines the phonon coupling and thus the heat transport across the interfaces. The coupling can be observed in evolution of phonon vibration in contacted nano-carbons. For example, between two parallel and infinite single-wall CNTs, the pre-excited breathing oscillation in one tube decays over a long time scale, while the breathing mode in the other tube becomes active, see Fig. 5A [94]. Such resonance effect allows near complete and highly efficient intertube energy transfer, and the strength of the intertube vdW interaction sets the time scale for the energy transfer. It is also found that the LFPs exchange energy more rapidly. However, in more cases, there are just finite contacts between CNTs, namely CNT junctions. Due to the limited contact length, the intertube coupling is weak and thus the thermal resistance of CNT junction is huge. For example, an interfacial conductance $G_{CNT-CNT}$ of 50 pW K^{-1} was obtained for crossing single-wall CNTs by using both MD and atomistic Green's function simulations [95]. By decreasing the spacing between CNT junctions to the coherence length of phonons, $G_{CNT-CNT}$ becomes one order of magnitude smaller, indicating that the interference effects and coherent transport of phonons play a significant role. For (10,10) CNTs, $G_{CNT-CNT}$ can vary from ~600 to ~100 pW K^{-1} with changing the crossing angle from 0° to 90° [22]. There is another contact between CNTs, namely overlapping. The heat transport across two overlapped CNTs can be affected by the nanotube spacing, overlap, and length, as shown in Fig. 5B [81]. By increasing the overlap and tube length, as well as decreasing the intertube spacing, the cross-plane heat transport can be efficiently enhanced. Note that the most dramatic enhancement of heat transfer is at a spacing smaller than 0.2 nm, where the heat transfer mechanism by bonded interactions is enabled. Furthermore, the large interfacial thermal resistance can be significantly reduced by modifying the molecular structure at the interface to enhance both the matching of phonon spectra and phonon mode coupling. The modification can be the increase in overlap length, strengthening in intertube coupling, polymer wrapping around the CNT junction, and metal coating [96]. There are also other essential parameters to govern the across-tube thermal conductance. For example, the number of walls and the associated curvature can determine the efficiency of thermal energy exchange [97,98]. From the point of view of anharmonicity of the interfacial interaction, it is revealed that inelastic effects become important at high temperatures and can facilitate the interfacial heat transfer [85].

As introduced above, the presence of a substrate can strongly suppress the in-plane heat transport in multi-layer graphene [76].

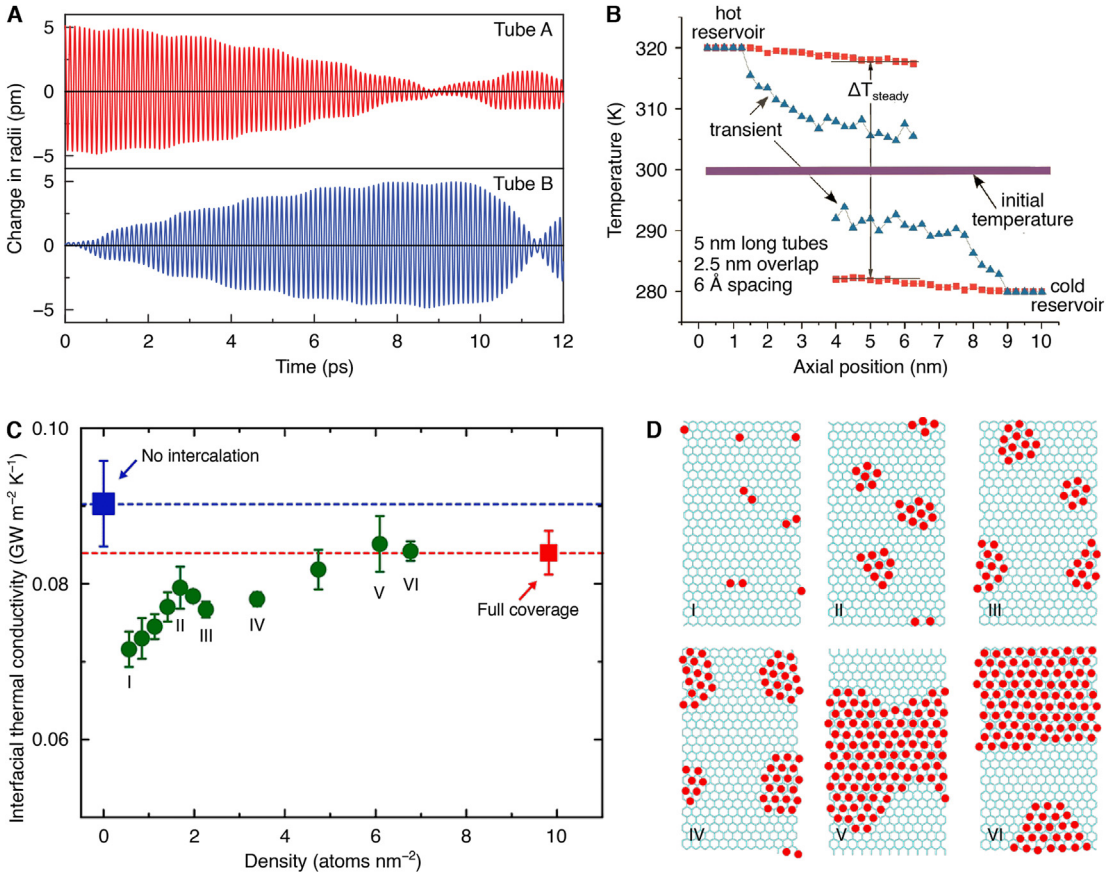

Fig. 5. Heat transport across the interface between nano-carbons. (A) Change in the radius of two parallel (10,0) CNTs (A and B) as a function of time, indicating the transfer of energy between them [94]. (B) Initial, transient, and steady-state temperature profiles for two 5 nm long (10,10) CNTs with 2.5 nm overlap and 0.6 nm spacing [81]. The outermost five data points at the left and right ends represent the temperatures imposed at the hot and cold reservoirs. The steady-state temperature jump in the overlap region corresponds to intertube thermal resistance. (C) Interfacial thermal conductivity for bilayer graphene intercalated with argon atoms, as a function of the areal density [25]. The conductivities without intercalation and with full coverage are also plotted for reference. (D) Snapshots (I–VI) of intercalated argon monolayers as areal density indicated in (C). (A colour version of this figure can be viewed online.)

However, the enhanced interfacial phonon coupling and energy exchange is the aim for designing efficient thermal-conductive interfaces between various 2D nanostructures. MD simulations have shown that the shearing phonon modes have different contribution to the interfacial heat transport [99]. The shearing modes account for about 15% and 39% of the total heat transport for the graphene/graphene and MoS_2/MoS_2 contacts, while the contribution is just 2% for the graphene/MoS_2 heterostructure. This is because the formation of periodic Moiré pattern in the heterostructure suspends the excitation of shearing modes. When defects are introduced in either graphene or MoS_2, they can break the Moiré pattern and thus increase the interfacial friction. Consequently, the interfacial phonon coupling, and thus the heat transport, are enhanced. Similarly, for the graphene/silicene heterostructure, there is a small lattice mismatching (~2.5%) for both layers [100]. The mismatching has a strong influence on the vibrational properties. Different from the free-standing graphene whose in-plane and out-of-plane phonons are well decoupled, the coupling with silicene induces breaking in various symmetries (e.g., reflection, translation, and rotation) of graphene, and thus the atomic vibrations are altered by the interfacial vdW interactions, leading to the coupling of in-plane and out-of-plane phonons. As temperature increases, the LFPs can be more scattered into multiple LFPs, which are coupled with the phonons in silicene (in a frequency range of 1–17 THz) to contribute the enhancement in interfacial thermal transport. When hydrogenation is applied on the graphene from the side facing the silicene, the Si–H interaction increases the strength of interfacial coupling and thus the heat transport. Similarly, for the conductance across a gold/graphene interface, the defects in the graphene sheet can enhance the out-of-plane LFPs in graphene, and thus improve the heat transfer across the interface [101].

Another way to deal with the phonon coupling is the across-interface phonon transmission and thus the transmission coefficient. For example, the average phonon transmission coefficient from a multi-layer graphene to the SiO_2 substrate was calculated to be about 0.2 at room temperature [76], providing another proof of coupling between the in-plane modes in graphene and the surface and bulk modes in SiO_2. It is also found that the intrinsic thermal conductance of most graphene/metal interfaces is only ≈50% of the phonon radiation limit, suggesting that heat is carried across the interfaces mainly through the elastic transmission of phonons [102]. To overcome the problem of a large mismatch in the phonon energy in graphene and the metals, metal nitrides can be used as replacement to enhance the inelastic phonon transport and provide better matching of phonon energy.

Furthermore, besides the above understanding of the interfacial phonon coupling, a new process of remote interfacial phonon (RIP) scattering is recently considered to be an important heat transfer mode at the interface between nano-carbons and dielectric substrates [103]. The RIP scattering arises from the thermally excited vibrational modes near the substrate surface (e.g., SiO_2) that have an electric dipole moment and can couple with the charge carriers

in nano-carbons [104–106]. However, unlike CNTs, the contribution of RIP in graphene/dielectric substrate is quite small (less than 2%) compared with that of phonon vibration. Such difference is due to the small contact area between CNT and substrate, while for the large contact area between graphene and substrate, the interfacial phonon coupling is the major part. Clearly, such RIP scattering can be considered a type of electron–phonon coupling.

The cross-plane heat transport can also be altered and even enhanced by introducing guest particles at the interfaces, due to the possible enhancement of phonon coupling by the LFPs of the guest particles. For example, argon intercalation shows a strong influence on the interfacial conductivity of bilayer graphene, see Fig. 5C and D [25]. At low concentrations, the conductivity is reduced by the intercalating atoms, as the coupling between different layers is suppressed. When the number of Ar atoms increases, a new atomic layer is formed between the graphene layers, resulting in the decrease in graphene–graphene coupling and rapid increase in Ar–graphene coupling. For a full coverage, the conductivity reaches the maximum, yet still smaller than that without intercalation. Nevertheless, by selecting appropriate intercalating guest particles, the interfacial heat transport can become stronger. For example, based on the successful MD studies on the thermal conductivity of graphene sheets [107,108], the diffusivity of the interface between GO and lipid membrane was investigated [109], showing that structured water can be identified near the GO layer with a maximum thickness of 1 nm. The intercalated and confined water can mediate the interfacial thermal coupling, and efficiently enhance the thermal dissipation. Similar to this study, an interface-engineering approach was designed to establish a seamless, electrically insulating, while thermally transparent interface between graphene and metal substrates by introducing water intercalation [110]. The presence of the interfacial water layer can expand and unfold the wrinkles formed on graphene sheets and insulate the electronic coupling, whereas the water vibrations still provide efficient pathways for interfacial heat transport.

There are other more efficient guest particles, such as nano-clusters and nanowires (NWs) which exhibit a high DOS for LFPs due to the surface effect and/or amorphous structure [111–114]. Therefore, when NWs are introduced between nano-carbons, the LFPs of nano-carbons can be strengthened, and the across-plane phonon scatterings (energy exchange) can be thus enhanced. In a model where an atomic Au chain is introduced between two adjacent CNTs, MD simulations showed that more local carbon atoms (of both CNTs) can vibrate at sub-5 THz [115]. Such increased DOS is ascribed to the resonance with the vibration of the Au atom chain which possesses abundant LFPs. Similarly, with a similar model where $(I_3)^-$ and $(I_5)^-$ polyiodide chains are intercalated between two adjacent CNTs, more local carbon atoms at the contacts are found to vibrate at frequencies <5 THz and around 12 and 20 THz, as the iodine atoms vibrate in an extremely low frequency region (<2 THz) [116]. Besides these, polymer wrapping can also provide additional pathways for heat transport of CNT junctions [96]. When ten polyethylene chains wrap around two adjacent CNTs, the hybrid structure shows vibrational modes at low frequency ranges, indicating an assisting role of polyethylene chains in energy transfer between CNTs.

3. Macroscopic nano-carbon assemblies

In the past decade, various macroscopic nano-carbon assemblies have been developed [117,118]. Among them, 3D foams, aerogels and forests, 2D films and sheets, and 1D fibers are of particular interests. In these assemblies, the utilization efficiency of the high thermal conductivity of individual nano-carbons is similar to the problem toward high strength and electrical conductivities. For example, high alignment and packing density are important to improve the tensile strength and electrical conductivity for CNT and graphene fibers [119–123]. Usually, they are also beneficial for thermal conductivity [3], and thus the thermal performance varies greatly according to the dimensionality of the assemblies, as they generally become loose to compact from 3D to 1D, and from entangled to aligned.

3.1. Experimental investigations

3.1.1. 3D aerogels, foams, and forests

3D aerogels and foams [124] are not good at heat conduction due to the suppressed conductivity contributed from the gas flow within the structural pores, thus their most possible applications are thermal insulators. For example, a very low κ of 0.0263 W m^{-1} K^{-1} at 200 °C was obtained for a carbon aerogel at a mass density of 0.066 g cm^{-3} [125], similar to the pioneering research of carbon aerogel (0.029 W m^{-1} K^{-1}) about 20 years ago [126,127]. Fig. 6A and B shows two SEM images for such carbon aerogels with a mass density of 0.052 and 0.182 g cm^{-3}, respectively. (The samples were obtained by carbonizing the supercritically dried resorcinol-formaldehyde aerogels.) Their sub-μm pores can efficiently suppress the gas convection for heat conduct. With increasing the mass density, the pore size gradually decreased (Fig. 6C), and the contribution of the intrinsic heat conduction between carbon particles was enhanced, as reflected by the increase in total conductivity (Fig. 6D).

The κ value can be much smaller when graphenes are assembled directly into aerogels. Ultralight graphene aerogels with a final density of 0.0141–0.0524 g cm^{-3} and pore size of tens to hundreds of μm were prepared by treating the freeze-dried graphene oxide (GO) aerogels with microwave heating [128] (The inset in Fig. 6E shows their self-assembled foam-like network with very thin cell walls.). As a result, the aerogels exhibited an extremely low κ of 0.0047–0.0059 W m^{-1} K^{-1} at room temperature, which further decreased at lower temperatures, see Fig. 6E. A slightly higher κ of 0.0281–0.0390 W m^{-1} K^{-1} for GO aerogels and 0.0363–0.0667 W m^{-1} K^{-1} for the 1500-°C-annealed ones were also reported, as their mass density was higher (0.0562 g cm^{-3}) [129]. In another study, due to the decreased pore size (about 3.6 nm), a porous graphene aerogel displayed $\kappa \approx 0.10$ W m^{-1} K^{-1} [130], yet still smaller than that of a polydimethylsiloxane (PDMS) film (0.18 W m^{-1} K^{-1}). The κ value became higher, up to 1.7 W m^{-1} K^{-1}, when the graphene aerogel was grown by chemical vapor deposition (CVD) on nickel foam [131], or up to 8.28 W m^{-1} K^{-1} on porous Al_2O_3 [132].

For CNTs, when being assembled into a 3D random network, the κ value is also down to ~0.1 W m^{-1} K^{-1}, smaller than that of thermally insulating amorphous polymers [95]. Such value is far below the conductivity of individual CNTs or single-layer graphenes, and also lower than that of other carbon-based TIMs [6,133,134]. The major reason is ascribed to the very low volume fraction of nano-carbons, the ultrahigh porosity of 3D nano-carbon monoliths, and the weak phonon coupling between neighboring nano-carbons via the very limited vdW contacts [95,131].

Another important 3D form of CNT assembly is the vertically aligned CNT array or forest. Due to the vertical alignment, the heat conduction along this direction can be much stronger as compared to the foams and aerogels. For example, a large anisotropy ratio as large as 72 was observed by measuring the longitudinal diffusivity (0.8 cm^2 s^{-1}) and the transverse one (0.011 cm^2 s^{-1}) [135]. The tested samples exhibited longitudinal κ in air of 3.0–6.4 W m^{-1} K^{-1} and transverse ones of 0.08–0.14 W m^{-1} K^{-1}. The longitudinal κ increased to 10–15 W m^{-1} K^{-1} for the annealed CNT forests, more than 3-fold higher than that of currently used phase-changing TIMs

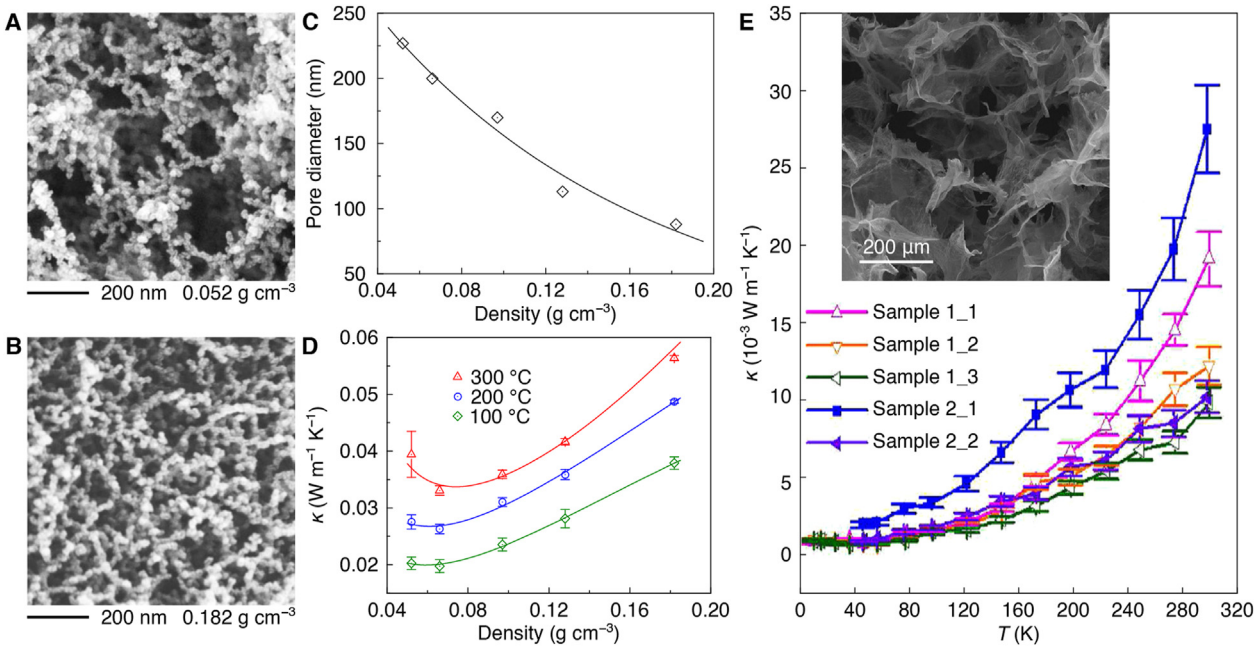

Fig. 6. Structure and thermal properties of carbon aerogels. (A,B) SEM images of carbon aerogels with a mass density of 0.052 and 0.182 g cm^{-3}, respectively [125]. (C,D) Pore sizes and total thermal conductivities of the aerogels as functions of mass density. (E) The measured thermal conductivity as functions of temperature for five graphene aerogels [128]. Inset shows the typical cellular structure of the aerogel. (A colour version of this figure can be viewed online.)

(2–5 W m^{-1} K^{-1}) [136]. Similar values along the length direction, e.g., 5.2–8.3 W m^{-1} K^{-1}, were also reported for more forests [137,138]. The conductivity strongly depends on the mass or tube density in the forest. For example, a longitudinal κ of 0.5–1.2 W m^{-1} K^{-1} was measured for ~6-mm high and 0.06-g cm^{-3} dense CNT forests [139], while by a dense growth, the mass density was ≈ 1.9 g cm^{-3} and the κ was 3.0–15 W m^{-1} K^{-1} [135]. Liquid soaking was used to make a solid of vertically aligned CNTs, resulting in a 15-fold increase in mass density [140]. The densified CNTs showed thermal diffusivities of 0.78–1.0 cm^2 s^{-1} at room temperature, while the values of the as-grown CNT forests were just 0.47–0.77 cm^2 s^{-1}. As a result, the typical κ value increased from 1.9 to 52 W m^{-1} K^{-1} after the densification. Today, in order to efficiently use CNT forests as TIMs, besides the growth of high-density CNT forests [135,141,142], metal coating [143] and shear pressing [86] on forest top have been used to reduce the contact resistance.

3.1.2. 2D mats, films, and papers

For the assemblies with denser packing densities, mostly in a 2D form (like a CNT mat or buckypaper), the in-plane conductivity becomes much higher, typically up to several to tens W m^{-1} K^{-1} [144–153], ascribed to the numerous intertube contacts. The situation is the same for other nano-carbon assemblies [129,154]. The key issues affecting the thermal properties are also the nano-carbon alignment and densification. For a multi-wall buckypaper with random CNT alignment, the in-plane κ was just up to 2.92 W m^{-1} K^{-1} [148], and the perpendicular (out-of-plane) one was quite similar, of 2.25 W m^{-1} K^{-1} [150]. In order to improve the κ value, Cu NWs were mixed into CNT buckypapers, and it was enhanced to 10.1 W m^{-1} K^{-1} at a CNT:Cu mass ratio of 1:1 [150]. Clearly, the random orientation and the corresponding low packing density limit strongly the thermal performances. Different from the filtration strategy that was used in the above buckypapers, nonwoven CNT films were also prepared by collecting CVD-grown CNT aerogels [155]. The nonwoven CNT films exhibited anisotropic properties along the in-plane and perpendicular directions, where the κ values were 25 and 0.1 W m^{-1} K^{-1}, respectively.

Improving CNT alignment can greatly enhance the heat transfer along the alignment direction. A comparison was conducted for the random aligned and magnetically aligned single-wall buckypapers, and their nanocomposites as well, see Fig. 7A and B [145]. The alignment increased the conductivity at 270 K from 16.2 to 32.1 W m^{-1} K^{-1}, and induced a high anisotropy of 1.64 between the conductivities along and perpendicular to the alignment direction. (The anisotropy was even up to 3.5 for temperature below 200 K) A notable result is that the perpendicular κ was close to that of random buckypapers, indicating that a certain number of CNT contacts can allow efficient heat transfer through the CNT network. However, for the buckypaper-based nanocomposites, the κ values became much lower (Fig. 7A and B), as the matrix (epoxy) has a low conductivity (0.2 W m^{-1} K^{-1}), and the infiltration also suppresses the intertube phonon coupling. For the denser and more magnetically aligned CNT films, the conductivity along the parallel direction could exceed 200 W m^{-1} K^{-1} [144,156]. By domino pushing aligned CNT forests and layer-by-layer stacking the forest-spun CNT sheets, much highly packed and aligned CNT films were obtained, which showed a high conductivity even up to 300–766 W m^{-1} K^{-1}, at a mass density of 1.34–1.39 g cm^{-3} [146,157]. These highly aligned CNT films also exhibited excellent electrical conductivity and Young's modulus.

Owing to the planar structure, the highly compacted (and ordered) graphene papers show a much higher thermal conductivity than CNT films. For example, graphene papers with a density of 1.13 g cm^{-3} were prepared by vacuum filtration, namely FGPs, and then converted into ultrathin papers with a higher density of 1.95 g cm^{-3} by annealing at 2800 °C for 2 h and compressing at 100 MPa, namely FCGPs [158]. Both the electrical and thermal conductivities (σ and κ) were remarkably improved by 3.5–5 folds after the annealing and compressing, up to 2.39 × 10^5 S m^{-1} and 1324 W m^{-1} K^{-1}, respectively. To better show the different thermal properties, the temperature profiles as a function of heating time is also shown in Fig. 7D. After being connected to a heater, the heat

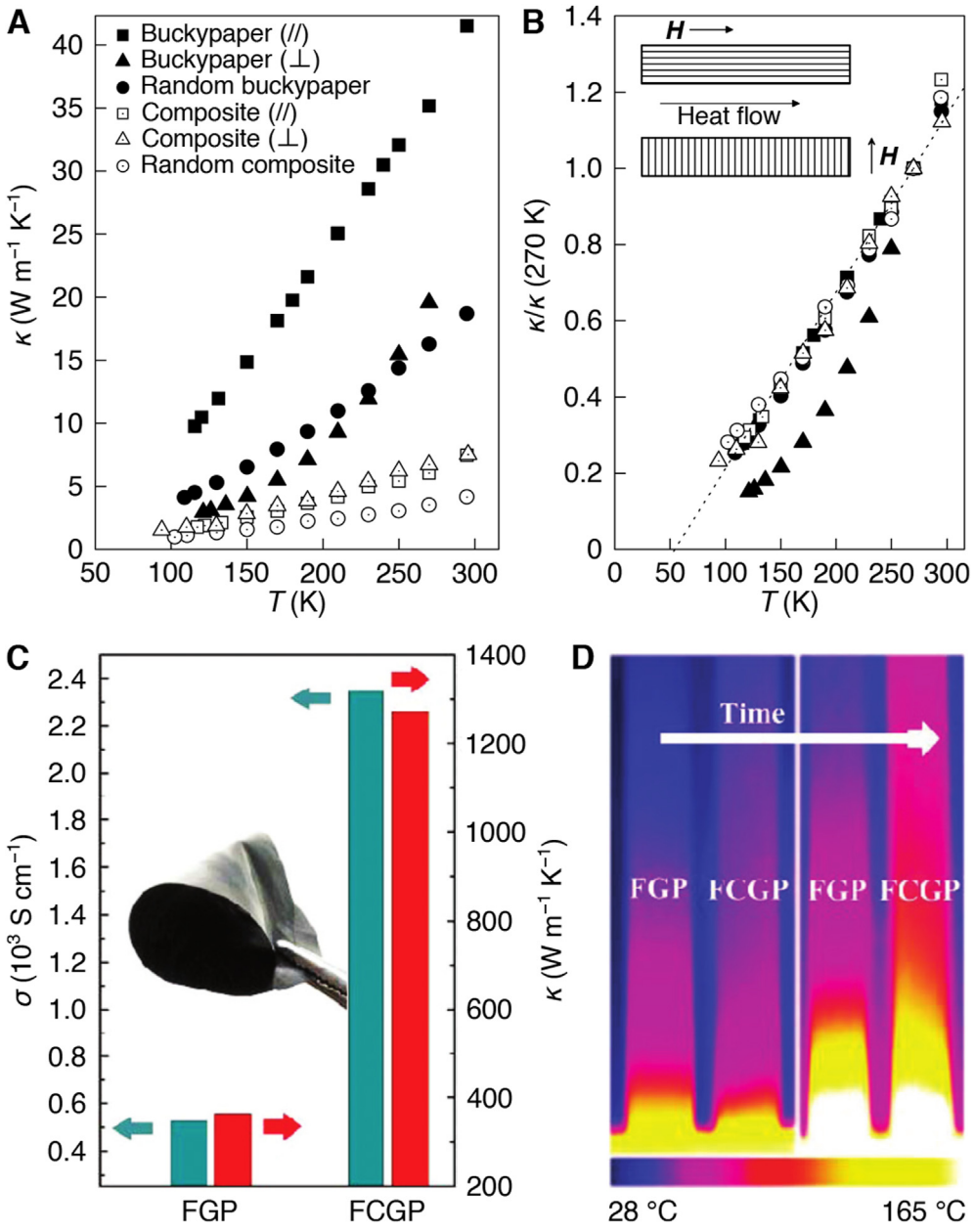

Fig. 7. Thermal properties of CNT and graphene papers. (A,B) Thermal conductivities and their normalized values for the pristine buckypapers and the corresponding composites along different directions [145]. Parallel (||) and perpendicular (⊥) indicate the heat flows which are parallel and perpendicular to the applied magnetic field direction (*H*) as shown in the inset. The normalization is based on the value obtained at 270 K. (C,D) Electrical and thermal conductivities of FGP and FCGP (the inset shows the tested FCGP), and IR images showing the temperature evolution of the heat spreaders made of FGP and FCGP, as a function of heating time [158]. (A colour version of this figure can be viewed online.)

transported much more rapidly along the FGCP film than the FGP. Interestingly, there is a switch-on effect of the thermal conductivity for graphene papers [159]. For a high-purity graphene paper (mass density 1.62 g cm^{-3}), the thermal conductivity could jump from 1732 to 3013 W m^{-1} K^{-1} when the temperature decreased from room temperature to 245–260 K. (The thermal diffusivity also jumped by several folds due to the switch-on.) This is caused by the difference in thermal expansion coefficient between the pure graphene flakes and surrounding impurity flakes, inducing separation of the flakes at certain temperatures.

Clearly, the 2D assemblies of CNTs and graphene sheets usually exhibit higher in-plane thermal conductivities than the perpendicular ones. The high degree of alignment or ordering of the nanocarbons, as well as the high packing density, are necessary for more efficient interfacial phonon coupling and thus the high in-plane conductivities. Due to the planar nano-structure, graphene papers are more conductive for heat than CNT films.

3.1.3. 1D fibers

Owing to the high alignment and densification, the 1D assembly of CNT fibers can also be very conductive for heat. So far, a wide range of value of 21–770 W m^{-1} K^{-1} has been reported for the conductivity. For example, a value of 60±20 W m^{-1} K^{-1} was reported for a 10-μm-diameter forest-spun CNT fiber at room temperature [160]. It was higher than that of 21 W m^{-1} K^{-1} for a wet-spun 0.5-μm CNT fiber [161]. There is generally a remarkable decrease in conductivity with increasing the fiber diameter; for a 34-μm sample the κ value decreased to below 30 W m^{-1} K^{-1}. Here

the loose packing of CNTs, as reflected by the fiber density of ~ 0.9 g cm^{-3}, strongly limited the thermal performance, due to the strong interfacial thermal resistance. By upgrading the wet-spinning method, multifunctional CNT fibers were prepared, that combined carbon fiber's high specific strength, stiffness, and thermal conductivity with metal's specific electrical conductivity [162]. Fig. 8A shows the CNTs were highly aligned and densified in these fibers. The CNTs bundled together to form thin fibrils with a diameter of 10–100 nm and length >50 μm, and these fibrils built up hundreds-of-meter-long fibers. The fibers had a high mass density up to 1.3 g cm^{-3}, as evidenced by the morphologies of fiber's cross section. As a result, the fibers exhibited a tensile strength of 1.0±0.2 GPa, modulus of 120±50 GPa, electrical conductivity $\sigma = (2.9 \pm 0.3) \times 10^6$ S m^{-1}, and thermal conductivity $\kappa = 380 \pm$ 15 W m^{-1} K^{-1}. Iodine doping could further improve the performance; the highest σ and κ values were 5×10^6 S m^{-1} and 635 W m^{-1} K^{-1}, respectively. Fig. 8B compares CNT fibers (from various literature) to the materials with the best electrical and thermal properties. These CNT fibers have combined the specific σ of metal wires (copper, silver, and aluminum) with the specific κ of high-performance carbon fibers.

For the measurement of 1D and 2D samples with one dimensionality in the micrometer scale, the heat radiation could be problematic by resulting in a large difference in the apparent and intrinsic (true) thermal conductivities (as discussed below). By revising the measurement method, it is possible to extract the true conductivity from the apparent one (κ_{ap}). For example, κ_{ap}. diverged with increasing the sample length for a neat CNT fiber (489, 504, and 584 W m^{-1} K^{-1} at fiber length of 7.19, 8.84, and 11.56 mm, respectively), while the true one was $\kappa = 448 \pm 61$ W m^{-1} K^{-1} by extracting the contribution of heat radiation. Thus based on the revised measurement, one can analyze the strategies tuning the thermal performances, and it is suggested to compare the true conductivity in fute investigations. For example, when a CNT fiber was infiltrated with polyvinyl alcohol, both κ_{ap} and κ decreased by about 30–50% ($\kappa = 225 \pm 15$ W m^{-1} K^{-1}), indicating that such polymer inhibited the heat transfer between CNT bundles. The conductivity can also be different by changing the spinning method. For an aerogel-spun CNT fiber, and obtained $\kappa = 75.9$ W m^{-1} K^{-1} at room temperature [164]. This is ascribed to the entangled CNT assembly and the residual catalyst particles. After a soaking treatment with HCl, the room temperature κ was improved up to 138 W m^{-1} K^{-1}, which was considered as a result of the removal of the residual particles.

Like the films/papers, graphene fibers also show a higher thermal conductivity than CNT fibers. Recently, graphene fibers with different microstructures were spun by using large- and small sized GO sheets (LGGOs and SMGOs) [163] (Fig. 8C shows the microstructures of an optimized fiber containing SMGOs.). For the pure LGGO fibers, microvoids were generated between graphene sheets during thermal annealing. After adding 30 wt% SMGOs, these voids were filled and the high degree of orientation of the LGGOs was well maintained inside the fibers. As a result, the annealed fibers containing SMGOs became much more conductive for both heat and electrons than the annealed LGGO fibers. Fig. 8D shows the effect of annealing temperature on κ for the two fibers. The optimized fiber containing 30 wt% SMGOs, subjected to annealing at 2850 °C, exhibited $\kappa = 1290 \pm 53$ W m^{-1} K^{-1} and $\sigma = 2.21 \pm 0.06 \times 10^5$ S m^{-1}. Besides the individual fibers, wet-spun GO fibers were used to fabricate nonwoven graphene fiber fabrics, where the crossed fibers can be self-fused to strengthen the fabrics and form efficient pathways for inter-fiber heat transfer. After being annealed at 3000 °C, the final fabrics exhibited a high in-plane $\kappa =$ 301.5 W m^{-1} K^{-1}.

Clearly, due to the different assembly structures, nano-carbon aerogels, foams, forests, mats, papers, fibers, and fiber fabrics have shown quite different thermal properties. The thermal conductivity is mainly determined by the capacity of heat transfer between different nano-carbon structures, and can range from below 0.01 to above 1000 W m^{-1} K^{-1}, spanning more than 5 orders of magnitude. Besides the annealing treatment that is widely used to remove oxygen-containing functional groups and increase the

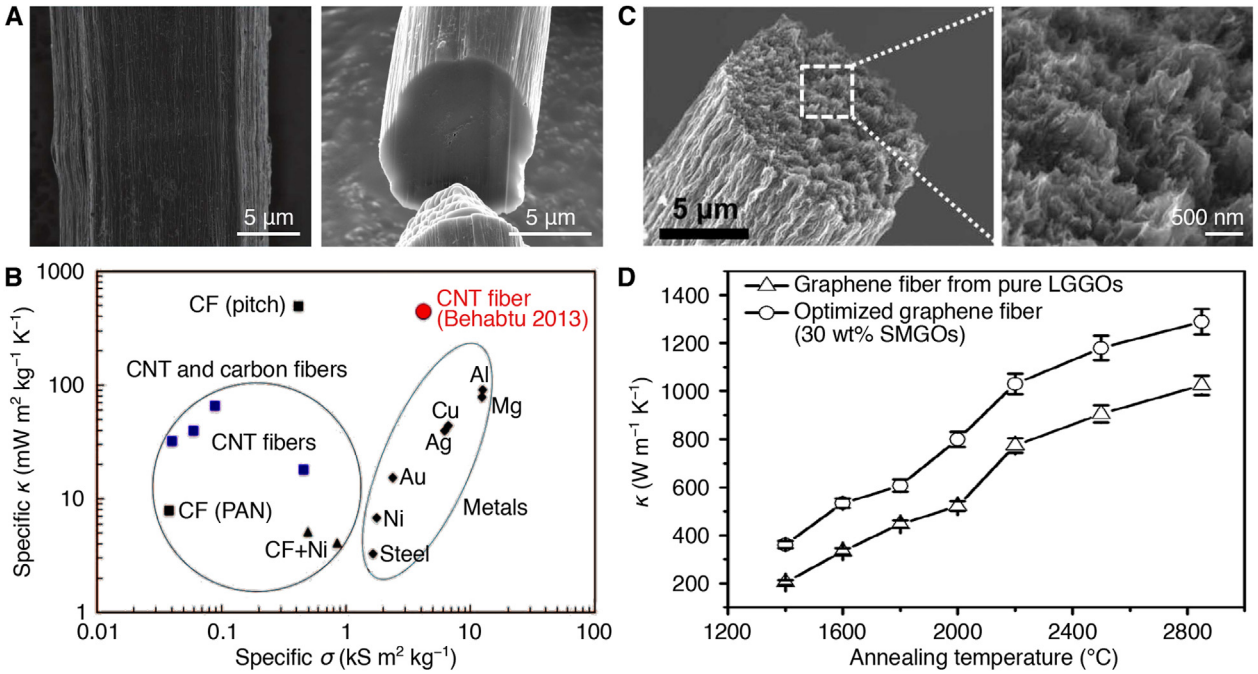

Fig. 8. Thermal conductivity of CNT fibers. (A,B) Structures and conductive properties of wet-spun CNT fibers [162].(C,D) SEM images of the optimized graphene fiber with 30 wt% SMGOs, and the comparison in thermal conductivity for graphene fibers without and with SMGOs [163]. (A colour version of this figure can be viewed online.)

sp^2 crystallinity, the most important problem is the appropriate design of the assembly structure, in which the phonon coupling between nano-carbons should be suspended or strengthened to meet the applications. Therefore, there are quite a number of strategies to improve the thermal performances.

3.2. Strategies to improve thermal performances

Acid treatment, densification, alignment optimization, etc., are found to be able to efficiently enhance the thermal conductivity of CNT fibers [165–167]. Thus far, the highest apparent conductivity κ_{ap} of 630–770 W m^{-1} K^{-1} (obtained at a gauge length of 2 cm) was obtained for an aerogel-spun fiber containing rich and densified single-wall CNTs, [167]. Local densification (e.g., using polar solvents) and short covalently bonding between CNTs (e.g., using acid treatments) are also effective to boost the interfacial conductance, with an enhancement factor of 2.8 [165]. In another strategy, Au nanoparticles were infiltrated into CNT fibers to excite sub-5-THz LFPs, resulting in the improved intertube heat transfer [115]. Such method can increase the intrinsic κ from to 30.5 to 50.0 W m^{-1} K^{-1}, by about 70%. Similarly, the decoration of I_3^- and I_5^- polyiodide chains can also excite the LFP modes for carbon atoms at the interfaces, and simultaneously act as extra heat transfer channels as well [116], similar to the iodine doping [162]. Furthermore, impregnation of metal nanoparticles [115] or NWs [168] can also improve the thermal conductivity by providing richer channels for intertube heat transfer. However, polymer infiltration that strengthens CNT fibers might not benefit the heat conduction as polymers are usually heat insulators. Nevertheless, it was still found that by applying electro curing on bismaleimide (BMI) resins which are pre-impregnated inside a CNT fiber, the cross-linked BMI molecular chains can be aligned along the CNTs, and thus enhance the heat conduction along and across the CNTs [169]. The apparent κ of electro-cured CNT/BMI fiber was up to 374 W m^{-1} K^{-1} (gauge length 12 mm), which is higher than that of various pure CNT fibers and sheets, and the intrinsic κ was even up to 177 W m^{-1} K^{-1}. A following investigation showed that the interaction between CNT and polymer and the effective heat transfer pathways are the key issues affecting the interfacial thermal transport [170].

For the graphene assemblies, the dry-bubbling process, graphitization, and mechanical pressing were used to improve the grain size and stacking order of graphene layers in their assembly films/papers [26]. The large grain size, high flatness, and reduced interfacial phonon scattering lead to remarkably enhanced thermal performances. The maximum κ of graphene films has reached to 3200 W m^{-1} K^{-1} and outperformed the commercial pyrolytic graphite sheet by 60%. By following the idea of incorporating SMGOs [163], a high κ value of 1103 W m^{-1} K^{-1} was obtained for the high-temperature annealed graphene films containing the same masses of LGGOs and SMGOs [171]. A decoration of Ag NWs into graphene nanosheets (reduced graphene oxide), realized by an in-situ growth, can also remarkably increase the across-plane conductivity by 260% [168]. Based on NEMD simulations, such improvement is derived from the strong excitation of LFP modes of the interfacial carbon atoms by resonating with Ag NWs.

Besides the intrinsic thermal properties of the nano-carbon assemblies, the contact resistance between them and the contacting substrates is also very important for applications. Usually it is also referred as “interface effect” to describe the contact resistance. For example, when CNT forests are used as TIMs, the interfacial transport between the forest and heat sink is still a challenging problem, where the forest’s degree of uniformity has become a key factor. By optimizing the CNT growth parameters (e.g., growth temperature and gas flow), the height uniformity was improved by 8 folds, and thus the contact resistance between CNT forest and heat sink was reduced by 60% [87]. Considering the limited contact between CNT ends and heat sink, an engineering method of shear pressing was designed to push the top CNT segments down to the horizontal direction [86]. Therefore, there became more contacts between the CNTs and heat sink (coated with SiO_2), resulting in a 7-fold increase in the in-plane thermal conductivity and a 4-fold decrease in the contact resistance. Moreover, the CNTs at the forest top were also coated with diamond-like carbon and/or TiN nanolayers to enlarge the contact area [172]. Such contact is more efficient for heat transport than the contact using the uncoated CNTs, and resulted in a 50-fold reduction in contact resistance (from 15 to 0.3 mm^2 kW^{-1}). These studies well demonstrate that the highly densified and flattened surface of nano-carbon assemblies are important for heat transport from the heat sink to the assemblies, or vice versa.

3.3. Theoretical investigations

For nano-carbon assemblies, predicting their thermal properties can be realized by theoretical models which take into account the assembly morphology, individual properties of nano-carbons, and the impact of their contacts [173] (Note that Section 2.3.1 discusses the principles of interfacial phonon coupling between two or several nano-carbons, while here the main focus is the modeling or simulation of the assembly containing massive nano-carbons.). Specially, the thermal phenomenon taking place at the contacts can also be investigated by Green’s function calculation.

For example, by considering the CNT-CNT contact conductance $G_{CNT-CNT}$ (the quantity can be well predicted by MD or Green’s function method), a formula is derived to describe the thermal conductivity κ_{mat} for randomly oriented CNT mat [174],

$$\kappa_{mat} = \frac{0.18L}{L_j^2} G_{CNT-CNT} \approx \frac{0.18L}{2\pi D} \frac{\rho_{film}}{\rho_{graphene}} G_{CNT-CNT}, \quad (2)$$

where L is the nanotube length, L_j the distance between CNT-CNT junctions, D the tube diameter, ρ_{film} the volumetric density of the CNT mat, and $\rho_{graphene} = 7.6 \times 10^{-7}$ kg m^{-2} the surface mass density of graphene. Based on such model, the conductivity in the dense limit is just approximately 5 W m^{-1} K^{-1}. This model is based on the assumption that the mean free path of phonons along the CNTs is long and that each CNT is at a uniform temperature, and thus the thermal conductivity of the assembly with random cross arrangement can be directly related to the mass density and $G_{CNT-CNT}$.

Later, a series of mesoscopic simulations on interconnected networks of CNT bundles were performed [175–177], where both the analytical expressions and numerical models were developed to predict the thermal performance of 2D and 3D CNT networks. For example, by using a soft-core approach, an expression for CNT film thermal conductivity was derived by assuming an infinite nanotube thermal conductivity [175]:

$$\kappa_{mat}^{\infty} = \frac{G_{CNT-CNT}}{D} \frac{n_V^2}{18}, \quad (3)$$

where n_V is the volume number density of CNTs. It indicates that the thermal conductivity of CNT films can vary by orders of magnitude depending on the CNT length and the assembly way (e.g., arrangement). This model was later extended to consider the finite nanotube thermal conductivity, leading to the following expression for the film conductivity [176]:

$$\kappa_{mat} = \frac{\kappa_{mat}^{\infty}}{1 + Bi_c\langle n_j\rangle/12} = \frac{\kappa_{mat}^{\infty}}{1 + Bi_T/12}, \quad (4)$$

where $Bi_T = Bi_c\langle n_j\rangle = G_{CNT-CNT}\langle n_j\rangle L/\kappa A$ is a Biot number comparing the total contact conductance from a nanotube to all of its contacts ($G_{CNT-CNT}\langle n_j\rangle$) to the intrinsic nanotube thermal conductance ($\kappa A/L$), $\langle n_j\rangle$ is the average number of junctions per nanotube, and A is the CNT's cross-sectional area. Based on this expression, two limits to the film conductivity were predicted: $\kappa_{mat} \propto \rho_{film}^2 L^2$ when $Bi_T \to 0$, and $\kappa_{mat} \propto \rho_{film}$ when $Bi_T \to \infty$. In other words, the thermal transport suggests a strong quadratic dependence on CNT length for these assemblies, and 3D assembly demonstrates much better thermal conductivity than the 2D one, due to the efficient heat transfer along the bundles. Clearly, these model investigations can clearly show a strong dependence on the assembly density and CNT length for the contribution of the finite tube conductivity to the real assembly materials.

MD simulations and atomistic Green's function calculations have also been used to investigate the thermal properties of nano-carbon assemblies. For example, the effects of various factors on the interfacial conductance between a CNT forest and Si substrate were simulated [90], such as the CNT arrangement, filling fraction, CNT diameter, and temperature. The results suggested that the filling fraction and arrangement of CNTs have the greatest impact on interfacial conductance; the aligned CNT forest is more conductive for interfacial thermal transport. However, as it consumes a huge amount of computational resources for large-size assemblies, the atomistic simulation is more widely used in the interfacial problems between nano-carbons, as already discussed above.

4. Thermal conductivity measurements

4.1. Measurement methods

The applicable measurement methods for the thermophysical properties of nano-carbon assemblies vary greatly according to the material's characteristic dimensions and the way to induce heat transport. Fig. 9A–H provides several methods that have been successfully used in recent years. Generally, 3D assemblies are comparatively easy to measure, and most commercial thermophysical measurement methods are quite applicable for samples with large dimensions. Among them, transient hot wire technique [178,179], hot disk method [180–182], laser flash method [140,183], and infrared thermal imaging technique [184,185] are the most common methods. The hot wire method (Fig. 9A) is a classical transient dynamical technique based on the measurement of the temperature rise of a linear heater/thermosensor embedded in the test materials, and from the temperature rise versus time curves, it is possible to derive the thermal conductivity [178]. This method is especially suitable for graphene nanopowders or nanofluids containing nano-carbon particles, because they are easy to cover the linear heater/thermosensor to complete the measurement. Likewise, the hot disk method (Fig. 9B) is another transient dynamical technique by means of planar heater/thermosensor encapsulated with insulating layers [180]. This change in sensor shape enable the hot disk method to measure the thermal conductivity of 3D nano-carbon bulks besides powders and fluids. In a marked contrast, the laser flash method (Fig. 9C) can only directly obtain the thermal diffusivity α instead of thermal conductivity, and the density ρ and specific heat capacity C_p are required to extract the thermal conductivity according to $\kappa = \alpha\rho C_p$ [140]. This method generally requires the samples to be squeezed into non-transparent disk shape with a certain thickness. Hence, it is only applicable to powder-squeezed disk structure for nano-carbons. For example, Craddock et al. [186] showed that it can be used to measure the thermal diffusivity of CNT bundles by filling them into a cylindrical heat-shrinkable tube, to form disk shape sample as well.

Compared with the 3D nano-carbon assemblies, the thermal conductivity characterizations of lower-dimensional nano-carbon materials, e.g., 2D films and 1D fibers, are more challenging. For the 2D ones, such as graphene monolayers and its assembled flakes, laser Raman spectroscopy method (Fig. 9D) is commonly used [187]. This is based on the phenomenon that materials will expand in volume when being heated, due to the change in bond length and bond angle, as reflected in the height and width of the corresponding characteristic Raman peaks [192,193]. Generally, when temperature increases, the Stokes Raman peak is red-shifted and widened, with the intensity decreased as well [194]. There have been several advanced Raman-based methods to measure the thermal properties of nano-carbons, such as the energy transport state resolved Raman method [194,195], frequency resolved Raman method [196], and time domain Raman method [197,198]. Balandin et al. [3,199] proposed the pioneering studies by using Raman spectroscopy to obtain κ for graphene materials. In the method, the κ value is related to the dependence between the frequency of Raman G peak and temperature, which is also a function of the excitation laser power. This is regarded as a milestone for the thermophysical property measurement because it achieved the κ measurement of sheet materials with an atomic thickness. The validity of the Raman method was further evaluated for graphene monolayers by considering the electron–phonon and phonon–phonon scattering rates [200]. In a marked contrast, for much thicker nano-carbon films, photothermal reflectance technology is a good approach, where a laser beam is focused on the sample surface and an infrared detector is used to receive the photothermal signals. According to the signals at different frequencies, the sample's thermal diffusivity can be obtained. It has been successfully used for multi-wall CNT forest films with a thickness of 10–50 μm [201].

An upgrade form of such method is named time-domain thermoreflectance (TDTR) method (Fig. 9E), which is based on the relationship between the light reflection coefficient and sample temperature [202]. Since a laser heats the sample in a very short time, the temperature change of the sample will appear abruptly and vanish rapidly, making it tough for phenomenon observation and data recording. The TDTR method solves this problem by converting the time domain into the space domain, where a mechanical delay stage is used to vary the optical path of the pump beam, producing a time delay between the pump excitation and probe sensing [203]. Thus far, the femtosecond laser detection technology has been integrated with the TDTR method; a sample is heated by a femtosecond laser to induce the change in temperature, and then the reflectance of the sample surface is measured in picosecond time. Fig. 9E shows an example for CNT forests, where the characteristic heating frequencies of TDTR (1–10 MHz) are used to probe heat transfer at length scales spanning ~0.1–1 μm, for measuring the contact resistance between the forest's free tips and an opposing substrate [188]. As more examples, the TDTR method was used to measure the contact resistance between highly ordered pyrolytic graphite and several metals, which are found to be similar to those of metal–diamond interfaces [204]; and the interfacial resistance of the multi-layer Au/Ti/graphene/SiO_2 interfaces was measured [205], showing that the transmission of phonons at the metal–graphene contact dominates while those at other contacts are negligible. Today, TDTR can also be used to reveal the anisotropic thermophysical properties by adjusting the laser spot size and modulation frequency [206].

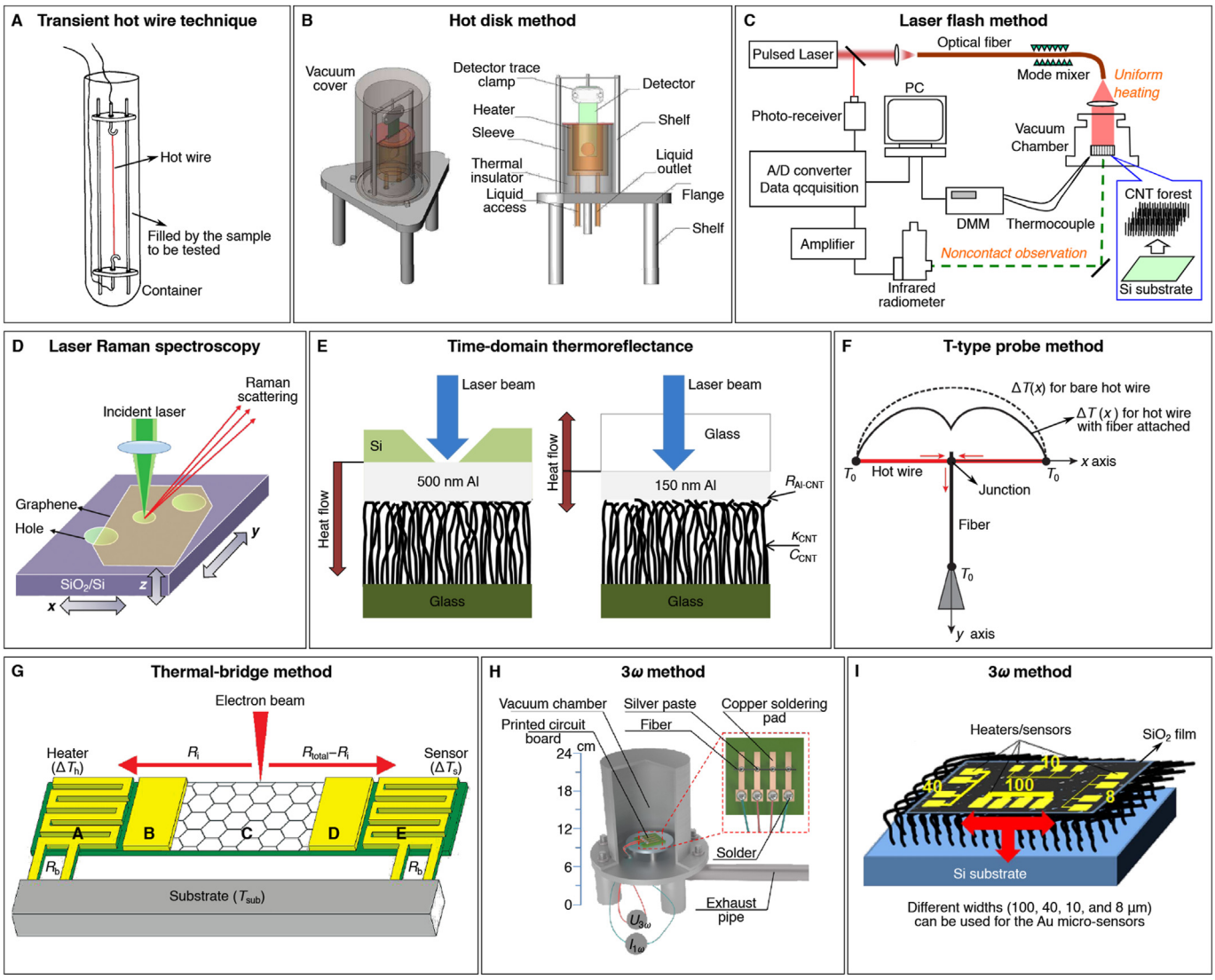

Fig. 9. Thermophysical characterization methods for nano-carbon assembly materials. A) Transient hot wire technique [178]. B) Hot disk method [180]. C) Laser flash method [140]. D) Laser Raman spectroscopy method [187]. E) Time-domain thermoreflectance [188]. F) T-type probe method [189]. G) Thermal-bridge method [190]. H,I) Two 3ω methods which have been used for CNT fiber [191] and CNT forest [86]. (A colour version of this figure can be viewed online.)

For the 1D nano-carbon materials, a micro-fabricated suspended device is developed to effectively obtain the κ value for a single CNT or nanofiber. In an early study, $\kappa \approx 1290$ W m^{-1} K^{-1} was measured at room temperature for a single-wall CNT by using this method [207]. Since then, various similar methods were developed, such as the suspended sample-attached T-type method [208], non-contact Raman spectra shift method [209–211], and laser flash method [186]. Among them, the T-type probe method (Fig. 9F) is a steady-state technology to obtain the thermal conductivity, where two different temperature distributions are stably formed along the hot wire when the tested fiber is connected or disconnected [189,212]. It is a very useful tool to simultaneously obtain the thermal conductivity, thermal diffusivity and heat capacity of an individual fiber.

A thermal-bridge method was also designed targeting at the characterization of NWs, nanotubes, and nanoribbons [213]. Fig. 9G [190] shows a schematic for this method, where two micro-electromechanical systems (MEMS) are employed as the heater and sensor, and linked with the thermal bridge (the tested sample, e.g., graphene). In such configuration, heat transfers from the heater A to the sample C and from C to the sensor E, and the phonon transport is impeded at the contacts B and D due to the sudden material and structural changes. Besides using Joule heating at the heater to establish a temperature gradient for thermal conductance measurement, a focused electron beam is used to induce localized heating, leading to additional heat flows in both directions to the heater and sensor. Therefore, the thermal conductivity of the sample can be evaluated after modeling and solving the different heat transfer processes. Such method was first developed to measure the conductivity of few-layer graphenes [190]. The results suggested that the flexural phonon modes contribute significantly to the thermal transport, and that owning to the phonon scattering at the contact interfaces, the apparent conductivity is generally lower than the theoretical one. However, although this method has been commonly used in measuring thermal conductivity of single or multi-layer 2D materials, there are still many problems and challenges [214]. The future improvements of the thermal bridge method may include: amelioration of the heater and sensor symmetry with the developed electron beam lithography and etching technique, a deeper analysis on the background thermal radiation

for the low conductivity measurement, and a more precise model to delineate the temperature distribution inside the MEMS, to extract the temperature at the contact point between sensor and sample.

The above-mentioned techniques are applicable for specific categories of nano-carbon assemblies, and some other methods are also occasionally used. For example, the non-contact Raman spectra shift method uses a modulated laser for sample heating and Raman excitation, and thus enables the average temperature rise to be measured synchronously [215]. The thermal diffusivity of individual CNT or CNT bundles [216] and the contact resistance at the CNT–CNT junctions [217] can be extracted by comparing the temperature increases induced by continuous laser and square-pulse laser heating without knowing the laser absorption coefficient.

Nevertheless, it is of great importance to develop methods that are applicable to materials with different dimensions, or applicable to measure the thermophysical properties of the same sample along different directions. For example, the steady-state infrared thermal metrology can be used to obtain κ for 1D CNT fibers and 2D films by monitoring their 1D/2D temperature profiles [166]. Another more efficient method, namely 3ω method, can realize the measurement of nearly all the 1D, 2D, and 3D nano-carbon assemblies by adopting various heat transfer models. For a single CNT, by inputting frequency-modulated alternating current into the nanotube, the third harmonic voltage ($U_{3\omega}$) is proved to be a very efficient and accurate function to extract the thermal conductivity and thermal diffusivity [218,219]. As shown in Fig. 9H, such 3ω method has been successfully applied for CNT fibers whose dimension (diameter) is in a range of several to tens of μm [191]. For 3D CNT film, multiple micro-sensors composed of four-pad metal strips are deposited on the film, and driven by alternating currents (Fig. 9I) [86]. Therefore, the in-plane and out-of-plane κ can be obtained by analyzing the third harmonic temperature profiles. The similar treatment is also used for 2D nano-carbon assemblies, where specially designed freestanding sensors are contacted on the top surface of a CNT forest. The thermal conductivities and interfacial resistances are thus obtained [87,172]. Thus far, the 3ω methods have become the most welcome strategy for nano-carbon materials due to the easy implementation, and there have been various upgrades and remedies specially for nano-carbon assemblies, as discussed below.

4.2. Scope of application

The various measurement methods have their own scopes of application. Fig. 10 summarizes the representative thermal conductivity data obtained from the above-mentioned methods, as a function of the characteristic dimension size of the nano-carbon materials. Clearly, the laser Raman spectroscopy method is very suitable for single-atom-thick graphene which possess extremely high thermal conductivity. The TDTR method is suitable for nano-carbon films with a thickness in the nanometer scale. For much thicker films, the photothermal reflectance method is an effective tool. When the sample dimension reaches the micrometer scale, the transient electro-thermal method, laser flash method, hot disk method, and 3ω method become applicable. Note that the values of thermal conductivity and sample length in MD simulations [220], specially for (10,10) single-wall CNTs, are also provided in Fig. 10.

From a different point of view, the T-type probe method is only applicable to individual nanotubes or 1D nano-carbon fibers; the transient hot wire technique is suitable for liquid materials and nano-carbon powders; and the TDTR method is more applicable for 2D nano-carbons. Fortunately, as mentioned above, the 3ω method shows the widest applicability as it can cover the nanotubes [221,222], fibers [169,223], films [224,225], bulks [226,227], foams [228], liquid [229,230], powders [231,232], and so forth. Importantly, it can even simultaneously extract the anisotropic thermal conductivities along different directions. Hence, the 3ω method might become the mainstream approach of thermophysical property measurement for nano-carbon materials.

4.3. 3-Omega method and its upgrade

The advanced compatibility of the 3ω method is owing to the adjustable penetration depth of the thermal wave. By changing the angular frequency ω of the alternating current, the penetration depth q can be continuously modulated according to $q^{-1} = \sqrt{\alpha/\omega}$. Generally, when the alternating current is conducted into a conductive strip, the strip's temperature is modulated at the double frequency 2ω by the Joule effect, and thus induces a 2ω-modulated electrical resistance $R = R_0(1 + \alpha_{CR}T)$, where R_0 is the room temperature resistance and α_{CR} is the temperature coefficient of resistance. Therefore, as a product of the current and resistance, the

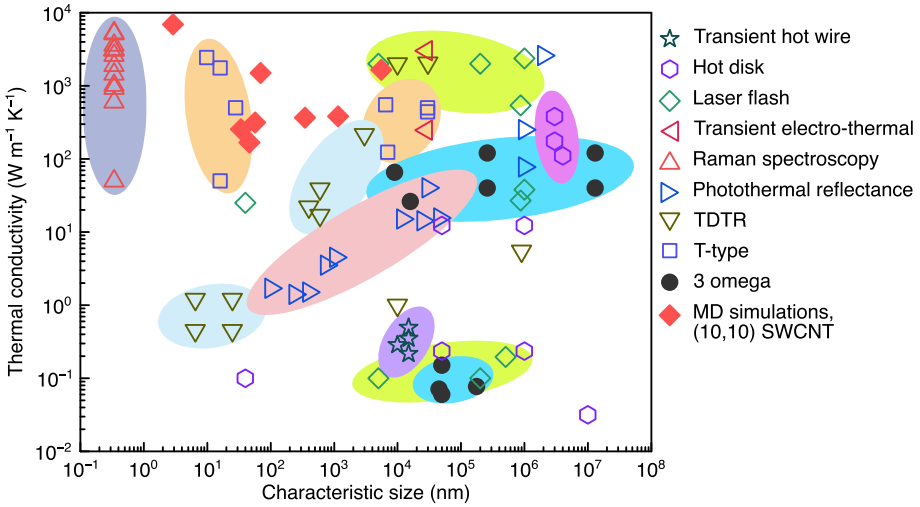

Fig. 10. Representative thermal conductivity data obtained from various characterization methods shown in Fig. 9 for nano-carbon materials. The MD results for (10,10) CNTs are also plotted, as summarized in Ref. [220]. (A colour version of this figure can be viewed online.)

strip's voltage contains harmonics of double and triple the base frequency, $U = U_0 + U_\omega + U_{2\omega} + U_{3\omega}$. Among them, $U_{3\omega}$ contains rich information of frequency-dependent thermophysical behaviors, even much better than the 2ω term.

By introducing a phase angle φ which is a function of the sample's thermal diffusivity α and the length L at which $U_{3\omega}$ is measured, namely $\tan\varphi \approx 2\omega L^2/\pi^2\alpha$, the 3ω voltage can be writteas

$$U_{3\omega} \approx \frac{4I_{\mathrm{rms}}^3 L R_0^2 \alpha_{\mathrm{CR}}}{\pi^4 S\kappa\sqrt{1+\tan^2\varphi}}, \tag{5}$$

where I_{rms} is the root-mean-square value of I and S is the cross-sectional area. Thus, by recording $U_{3\omega}$ at different frequencies, the conductivity κ and the characteristic thermal time constant $\gamma = L^2/\pi^2\alpha$ can be extracted. Note that the above analysis is based on 1D samples, such as metal wires, individual CNTs, and CNT fibers. For the application in richer forms of nano-carbon assemblies, it is necessary to introduce a certain modification or upgrades to the 3ω methods.

When the 3ω technique is introduced to nano-carbon assemblies, the corrugated assembly surface makes it difficult to apply the conventional sensor-deposited-on-material scheme. In order to precisely predict the intrinsic thermal conductivity of nano-carbon assemblies, it is important to design an appropriate contact between the heat source/sink or sensors and the nano-carbon materials. In a revised 3ω technique, originally by Hu et al. [222], a reasonable consideration of thermal resistances between various contacts/interfaces is developed to solve such problem for CNT forest. As shown in Fig. 11A, the equivalent thermal circuit involves various thermal resistances and capacitances for CNT forest, silicon substrate (on which CNT forest is grown), and SiO_2 substrate (on which microsensors are deposited with a subsequent covering of a passivation layer). According to this model, the total equivalent thermal impedance $Z_t(\omega)$ can be calculated as

$$\frac{1}{Z_t(\omega)} = \frac{1}{R_c + 1/\left[(R_{\mathrm{CNT}} + Z_{\mathrm{Si}}(\omega))^{-1} + j\omega C_{\mathrm{CNT}}\right]} + \frac{1}{Z_{\mathrm{SiO_2}}(\omega)}, \tag{6}$$

where R_c is the thermal contact resistance between CNT forest and SiO_2 passivation layer. Therefore, by fitting the experimental data at variable frequencies, both the effective thermal properties of the CNT sample and the thermal contact resistance can be subtracted. Such method was used to measure the conductivity of CNT forests, which is in a range of 74–83 W m^{-1} K^{-1} [222]. Based on this study, the contact between CNT forest and 3ω sensors was revised by using polymethylmethacrylate (PMMA) as the substrate and silicon nitrides as the passivation layer [87]. The softness of PMMA ensured a tight and full contact and a better operation process. Furthermore, the size of the sensor can be further reduced for a wider range of applications. By using such revised method, it was revealed that the thermal conductivity was improved up to 170 W m^{-1} K^{-1} for a forest whose CNTs contained dispersed Fe nanoparticles and were cleaner on forest top by avoiding the formation of carbonaceous byproducts.

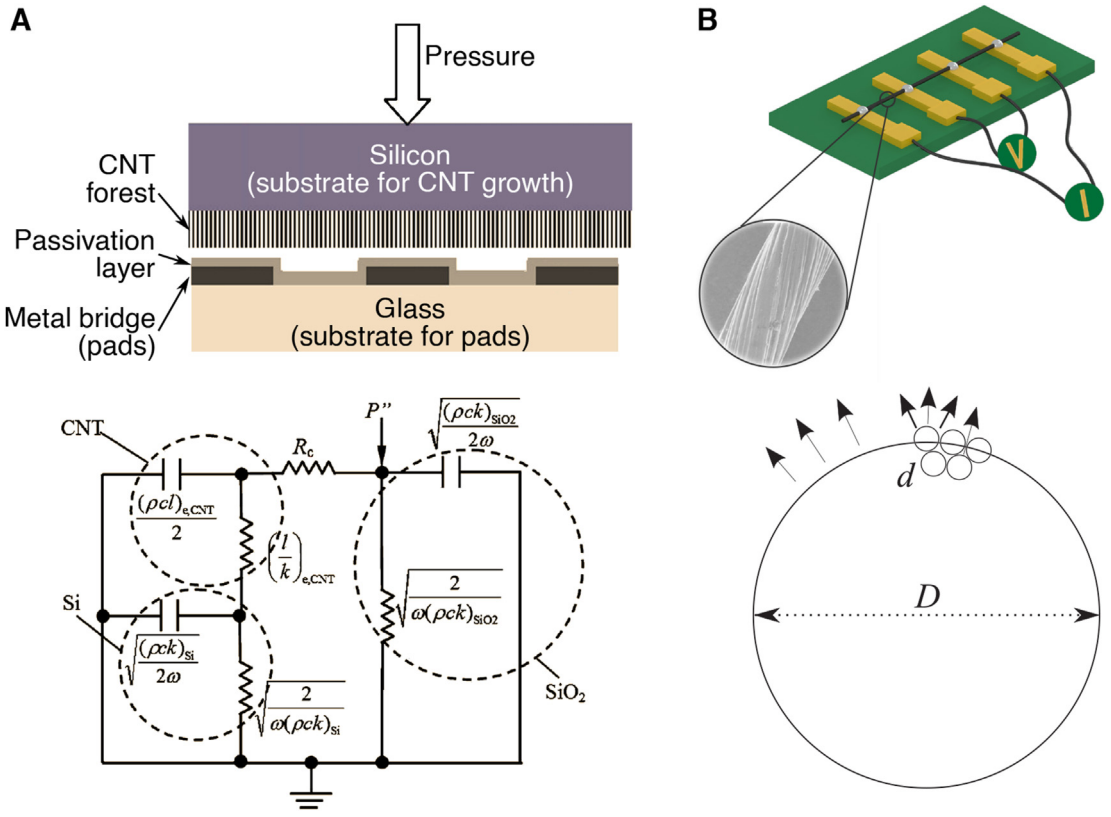

Fig. 11. Equivalent thermal circuits and thermal radiation model in the 3ω methods applied for nano-carbon assemblies. (A) Experimental set-up and the equivalent thermal circuit for the measurement for CNT forest [222]. ρ, c, k, and l are the density, specific heat, thermal conductivity, and thickness of the corresponding material, the subscript "e", denotes effective physical quantities, P'' is the applied power density, R_c is the contact thermal resistance, and ω is the frequency. (B) Schematics of the 3ω measurement for CNT fiber and the surface structure for heat radiation [169]. The surface of a D-diameter CNT fiber is covered by d-diameter CNT bundles. The bundle number on the surface is $N = \pi D/d$. If all the surfaces radiate heat, the total surface (circumference) should be $N\pi d = \pi^2 D$. If the second layer also radiates heat, the total circumference should be doubled, namely $2\pi^2 D$, and so on. (A colour version of this figure can be viewed online.)

Another way is to remedy the theoretical analysis to meet the special requirement from the nano-carbon assemblies. For example, as compared to solid 1D fiber, the assembly feature of CNT fiber provides more efficient heat radiation from the fiber surface. For the former, e.g., carbon fiber, due to the solid structure and smooth fiber surface, the apparent axial thermal conductivity is nearly a constant with increasing the fiber length, indicating that the radiation heat loss is small and even negligible. In a marked contrast, the apparent axial thermal conductivity of CNT fiber renders an obvious quadratic dependence on the fiber length, ascribing to the radiation heat loss from the outermost few layers of CNT bundles in the fiber surface. Therefore the relationship between the apparent and intrinsic (true) conductivities (κ_{ap} and κ) was reconsidered [169], which is presently established based on a cylindrical rod with a diameter D,

$$\kappa_{ap} = \kappa + \frac{16\varepsilon\sigma T_0^3 L^2}{\pi^2 D}, \tag{7}$$

where ε is the emissivity, ≈ 1 for porous carbon materials, $\sigma = 5.67 \times 10^{-8}$ W m^{-2} K^{-4} is the Stefan–Boltzmann constant, and T_0 is the measurement temperature. However, the surface of a CNT fiber is covered by small-size CNT bundles, and the radiation heat loss should be a sum of the contributions from these surface CNT bundles. By assuming an average bundle size (diameter) of d ($\ll D$), and taking the surface twist angle as zero (the effect on heat radiation is negligible), the cross section of the fiber is shown in Fig. 11B. Thus different from the cylindrical rod whose circumference is πD, the circumference for heat radiation in CNT fiber is about $C(D) = n\pi^2 D$, by considering that the n-th layer of CNT bundles in the fiber surface still radiates heat. Therefore, Eq. (7) can be revised as

$$\kappa_{ap} = \kappa + \frac{16\varepsilon\sigma C(D) T_0^3 L^2}{\pi^3 D^2}. \tag{8}$$

Clearly, as the diameter D is known, we can use Eq. (8) to estimate the real circumference around CNT fiber, which is very important when the fiber surface is quite porous.

By using the revised equation (Eq. (8)) to investigate various CNT fibers, it was found that the number of radiation layers (n) could be up to 4–10 for not-highly densified aerogel-spun CNT fibers, and was just about 0.26 for a smooth and highly densified forest-spun CNT fiber [169]. When BMI is impregnated into the aerogel-spun fibers, and then cured by an electro-heating strategy, n decreased to ≈ 3. Therefore, one can find a way to quantitatively connect the heat radiation to the structure and morphology of a fiber. Furthermore, based on this understanding, one can also more precisely distinguish the intrinsic conductivity from the apparent one. For CNT fibers, at a short fiber length of 2 mm, the two conductivities are nearly the same, $\kappa \approx \kappa_{ap}|_{L=2mm}$, and for the aerogel-spun CNT fibers κ could be improved from 30.0 to 177.3 W m^{-1} K^{-1} by the electro curing of impregnated BMI.

From the above investigations on nano-carbon assemblies, it becomes clear that there might be problems by the direct application of the 3ω strategy. Due to the increased number of interfaces, more complicated surface morphology, and thus the different heat radiation and/or heat capacitance, it is of great importance to revise/upgrade both the theoretical model and experimental technique to better evaluate the thermal properties of nano-carbon assemblies.

5. Conclusion

In the paper recent advances on the thermal transport in nano-carbon assemblies are reviewed, especially by focusing on the interfacial heat transport. For these materials, the interface-induced barrier for thermal transport is the most important problem that requires to be solved from both theoretical and experimental aspects. Based on the understanding of the effect of LFPs and interfacial phonon coupling of nano-carbons, a series of approaches to improve thermal conductivity have been proposed for nano-carbon assemblies. Among them the alignment optimization, physical densification, co-assembling of 1D and 2D nano-carbons, chemical modification on interfaces, and so forth, have shown great remarkable advantages. Furthermore, still considering the assembly feature, the rich areas of interface and complicated surface morphology have also introduced problems in the measurement methods both in the technical and theoretical point of views. By reviewing the various techniques successfully applied for nano-carbon assemblies, the recent developments in the 3ω method are also presented. Thus far, a great number of achievements have been realized for the mechanical and electrical properties for nano-carbon assemblies, whereas more efforts are still necessary for the high utilization of the intrinsically high thermal conductivity from the individual nano-carbon to the macroscopic assembly.

CRediT authorship contribution statement

Lin Qiu: Writing – original draft, Preparation, creation and/or presentation of the published work. **Xiaohua Zhang:** Conceptualization, Preparation, creation and/or presentation of the published work, Writing – original draft, Writing – review & editing. **Zhixin Guo:** Writing – original draft, Preparation, creation and/or presentation of the published work. **Qingwen Li:** Conceptualization, Writing – review & editing.

Declaration of competing interest

The authors declare that they have no known competing financial interests or personal relationships that could have appeared to influence the work reported in this paper.

Acknowledgement

This work was supported by the National Natural Science Foundation of China (51876008, 51862036, 21773293, 12074301), Beijing Natural Science Foundation (3202020), Fundamental Research Funds for the Central Universities (2232021G-01), Jiangxi Provincial Department of Science and Technology (20192BBE50031), and Science Fund for Distinguished Young Scholars of Hunan Province (2018JJ1022).

References

[1] J. Hone, M. Whitney, C. Piskoti, A. Zettl, Thermal conductivity of single-walled carbon nanotubes, Phys. Rev. B 59 (1999) R2514–R2516.
[2] S. Berber, Y.-K. Kwon, D. Tománek, Unusually high thermal conductivity of carbon nanotubes, Phys. Rev. Lett. 84 (2000) 4613–4616.
[3] A.A. Balandin, S. Ghosh, W. Bao, I. Calizo, D. Teweldebrhan, F. Miao, C.N. Lau, Superior thermal conductivity of single-layer graphene, Nano Lett. 8 (2008) 902–907.
[4] Z. Guo, D. Zhang, X.-G. Gong, Thermal conductivity of graphene nanoribbons, Appl. Phys. Lett. 95 (2009) 163103.
[5] A.A. Balandin, Thermal properties of graphene and nanostructured carbon materials, Nat. Mater. 10 (2011) 569–581.
[6] L.F.C. Pereira, I. Savić, D. Donadio, Thermal conductivity of one-, two- and three-dimensional sp^2 carbon, New J. Phys. 15 (2013) 105019.
[7] N. Yang, G. Zhang, B. Li, Violation of Fourier's law and anomalous heat diffusion in silicon nanowires, Nano Today 5 (2010) 85–90.
[8] N. Yang, X. Xu, G. Zhang, B. Li, Thermal transport in nanostructures, AIP Adv. 2 (2012), 041410.
[9] S. Lepri, R. Livi, A. Politi, Heat conduction in chains of nonlinear oscillators, Phys. Rev. Lett. 78 (1997) 1896–1899.

[10] B. Hu, B. Li, H. Zhao, Heat conduction in one-dimensional chains, Phys. Rev. E 57 (1998) 2992–2995.
[11] S. Maruyama, A molecular dynamics simulation of heat conduction in finite length SWNTs, Physica B 323 (2002) 193–195.
[12] G. Zhang, B. Li, Thermal conductivity of nanotubes revisited: effects of chirality, isotope impurity, tube length, and temperature, J. Chem. Phys. 123 (2005) 114714.
[13] X. Xu, L.F.C. Pereira, Y. Wang, J. Wu, K. Zhang, X. Zhao, S. Bae, C.T. Bui, R. Xie, J.T.L. Thong, B.H. Hong, K.P. Loh, D. Donadio, B. Li, B. Özyilmaz, Length-dependent thermal conductivity in suspended single-layer graphene, Nat. Commun. 5 (2014) 3689.
[14] J.X. Cao, X.H. Yan, Y. Xiao, J.W. Ding, Thermal conductivity of zigzag single-walled carbon nanotubes: role of the umklapp process, Phys. Rev. B 69 (2004), 073407.
[15] L. Lindsay, D.A. Broido, N. Mingo, Lattice thermal conductivity of single-walled carbon nanotubes: beyond the relaxation time approximation and phonon-phonon scattering selection rules, Phys. Rev. B 80 (2009) 125407.
[16] D.L. Nika, S. Ghosh, E.P. Pokatilov, A.A. Balandin, Lattice thermal conductivity of graphene flakes: comparison with bulk graphite, Appl. Phys. Lett. 94 (2009) 203103.
[17] S. Ghosh, W. Bao, D.L. Nika, S. Subrina, E.P. Pokatilov, C.N. Lau, A.A. Balandin, Dimensional crossover of thermal transport in few-layer graphene, Nat. Mater. 9 (2010) 555–558.
[18] L. Lindsay, D.A. Broido, N. Mingo, Diameter dependence of carbon nanotube thermal conductivity and extension to the graphene limit, Phys. Rev. B 82 (2010a) 161402.
[19] L. Lindsay, D.A. Broido, N. Mingo, Flexural phonons and thermal transport in graphene, Phys. Rev. B 82 (2010b) 115427.
[20] J.H. Seol, I. Jo, A.L. Moore, L. Lindsay, Z.H. Aitken, M.T. Pettes, X. Li, Z. Yao, R. Huang, D. Broido, N. Mingo, R.S. Ruoff, L. Shi, Two-dimensional phonon transport in supported graphene, Science 328 (2010) 213–216.
[21] J. Che, T. Çagin, W.A. Goddard, Thermal conductivity of carbon nanotubes, Nanotechnology 11 (2000) 65–69.
[22] W.J. Evans, M. Shen, P. Keblinski, Inter-tube thermal conductance in carbon nanotubes arrays and bundles: effects of contact area and pressure, Appl. Phys. Lett. 100 (2012) 261908.
[23] H. Song, J. Liu, B. Liu, J. Wu, H.-M. Cheng, F. Kang, Two-dimensional materials for thermal management applications, Joule 2 (2018) 442–463.
[24] P.E. Hopkins, M. Baraket, E.V. Barnat, T.E. Beechem, S.P. Kearney, J.C. Duda, J.T. Robinson, S.G. Walton, Manipulating thermal conductance at metal-graphene contacts via chemical functionalization, Nano Lett. 12 (2012) 590–595.
[25] H. Wang, J. Gong, Y. Pei, Z. Xu, Thermal transfer in graphene-interfaced materials: contact resistance and interface engineering, ACS Appl. Mater. Interfaces 5 (2013) 2599–2603.
[26] N. Wang, M.K. Samani, H. Li, L. Dong, Z. Zhang, P. Su, S. Chen, J. Chen, S. Huang, G. Yuan, X. Xu, B. Li, K. Leifer, L. Ye, J. Liu, Tailoring the thermal and mechanical properties of graphene film by structural engineering, Small 14 (2018) 1801346.
[27] S. Mohammad Nejad, M. Bozorg Bigdeli, R. Srivastava, M. Fasano, Heat transfer at the interface of graphene nanoribbons with different relative orientations and gaps, Energies 12 (2019) 796.
[28] B. Kumanek, D. Janas, Thermal conductivity of carbon nanotube networks: a review, J. Mater. Sci. 54 (2019) 7397–7427.
[29] S. Maruyama, A molecular dynamics simulation of heat conduction of a finite length single-walled carbon nanotube, Microscale Thermophys. Eng. 7 (2003) 41–50.
[30] N. Mingo, D.A. Broido, Length dependence of carbon nanotube thermal conductivity and the “problem of long waves”, Nano Lett. 5 (2005) 1121–1225.
[31] W.J. Evans, L. Hu, P. Keblinski, Thermal conductivity of graphene ribbons from equilibrium molecular dynamics: effect of ribbon width, edge roughness, and hydrogen termination, Appl. Phys. Lett. 96 (2010) 203112.
[32] Q.-W. Hou, B.-Y. Cao, Z.-Y. Guo, Thermal conductivity of carbon nanotube: from ballistic to diffusive transport, Acta Phys. Sin. 58 (2009) 7809–7814.
[33] J.A. Thomas, R.M. Iutzi, A.J.H. McGaughey, Thermal conductivity and phonon transport in empty and water-filled carbon nanotubes, Phys. Rev. B 81 (2010), 045413.
[34] A. Lippi, R. Livi, Heat conduction in two-dimensional nonlinear lattices, J. Stat. Phys. 100 (2000) 1147–1172.
[35] L. Yang, P. Grassberger, B. Hu, Dimensional crossover of heat conduction in low dimensions, Phys. Rev. E 74 (2006), 062101.
[36] L. Wang, B. Hu, B. Li, Logarithmic divergent thermal conductivity in two-dimensional nonlinear lattices, Phys. Rev. E 86 (2012), 040101.
[37] O. Narayan, S. Ramaswamy, Anomalous heat conduction in one-dimensional momentum-conserving systems, Phys. Rev. Lett. 89 (2002) 200601.
[38] X. Gu, Y. Wei, X. Yin, B. Li, R. Yang, Colloquium: phononic thermal properties of two-dimensional materials, Rev. Mod. Phys. 90 (2018), 041002.
[39] D.L. Nika, E.P. Pokatilov, A.S. Askerov, A.A. Balandin, Phonon thermal conduction in graphene: role of Umklapp and edge roughness scattering, Phys. Rev. B 79 (2009) 155413.
[40] D.L. Nika, A.S. Askerov, A.A. Balandin, Anomalous size dependence of the thermal conductivity of graphene ribbons, Nano Lett. 12 (2012) 3238–3244.
[41] V.N. Popov, C. Van Alsenoy, Low-frequency phonons of few-layer graphene within a tight-binding model, Phys. Rev. B 90 (2014) 245429.
[42] M. Damnjanović, E. Dobardžić, I. Milošević, T. Vuković, B. Nikolić, Lattice dynamics and symmetry of double wall carbon nanotubes, New J. Phys. 5 (2003) 148.
[43] R. Nicklow, N. Wakabayashi, H.G. Smith, Lattice dynamics of pyrolytic graphite, Phys. Rev. B 5 (1972) 4951–4962.
[44] M. Mohr, J. Maultzsch, E. Dobardžić, S. Reich, I. Milošević, M. Damnjanović, A. Bosak, M. Krisch, C. Thomsen, Phonon dispersion of graphite by inelastic x-ray scattering, Phys. Rev. B 76 (2007), 035439.
[45] Z. Yao, J.-S. Wang, B. Li, G.-R. Liu, Thermal conduction of carbon nanotubes using molecular dynamics, Phys. Rev. B 71 (2005), 085417.
[46] A.I. Cocemasov, D.L. Nika, A.A. Balandin, Engineering of the thermodynamic properties of bilayer graphene by atomic plane rotations: the role of the out-of-plane phonons, Nanoscale 7 (2015) 12851–12859.
[47] K.N. Anindya, M.S. Islam, J. Park, A.G. Bhuiyan, A. Hashimoto, Interlayer vacancy effects on the phonon modes in AB stacked bilayergraphene nanoribbon, Curr. Appl. Phys. 20 (2020) 572–581.
[48] K. Sääskilahti, J. Oksanen, S. Volz, J. Tulkki, Frequency-dependent phonon mean free path in carbon nanotubes from nonequilibrium molecular dynamics, Phys. Rev. B 91 (2015) 115426.
[49] M.N. Luckyanova, J. Garg, K. Esfarjani, A. Jandl, M.T. Bulsara, A.J. Schmidt, A.J. Minnich, S. Chen, M.S. Dresselhaus, Z. Ren, E.A. Fitzgerald, G. Chen, Coherent phonon heat conduction in superlattices, Science 338 (2012) 936–939.
[50] A.I. Cocemasov, D.L. Nika, A.A. Balandin, Phonons in twisted bilayer graphene, Phys. Rev. B 88 (2013), 035428.
[51] J. Wu, H. Xu, W. Mu, L. Xie, X. Ling, J. Kong, M.S. Dresselhaus, J. Zhang, Observation of low-frequency combination and overtone Raman modes in misoriented graphene, J. Phys. Chem. C 118 (2014) 3636–3643.
[52] S.-Y. Yue, T. Ouyang, M. Hu, Diameter dependence of lattice thermal conductivity of single- walled carbon nanotubes: study from ab initio, Sci. Rep. 5 (2015) 15440.
[53] D. Chalin, M. Avramenko, A. Parmeggiani, S. Rochal, Low-frequency phonon dynamics and related thermal properties of axially stressed single-walled carbon nanotubes, J. Phys. Condens. Matter 31 (2019) 425302.
[54] H. Suzuura, T. Ando, Phonons and electron-phonon scattering in carbon nanotubes, Phys. Rev. B 65 (2002) 235412.
[55] X.H. Zhang, G.E. Santoro, U. Tartaglino, E. Tosatti, Dynamical phenomena in fast sliding nanotube models, Philos. Mag. 93 (2013) 922–948.
[56] A.J. Pool, S.K. Jain, G.T. Barkema, Structural characterization of carbon nanotubes via the vibrationaldensity of states, Carbon 118 (2017) 58–65.
[57] A.H. Howlader, M.S. Islam, S. Tanaka, T. Makino, A. Hashimoto, Vacancy and curvature effects on the phonon properties of single wall carbon nanotube, Jpn. J. Appl. Phys. 57 (2018), 02CB08.
[58] C. Cong, T. Yu, Enhanced ultra-low-frequency interlayer shear modes in folded graphene layers, Nat. Commun. 5 (2014) 4709.
[59] N.A. Roberts, D.G. Walker, A review of thermal rectification observations and models in solid materials, Int. J. Therm. Sci. 50 (2011) 648–662.
[60] X. Ran, Y. Guo, Z. Hu, M. Wang, Interfacial phonon transport through Si/Ge multilayer film using Monte Carlo scheme with spectral transmissivity, Front. Energy Res. 6 (2018) 28.
[61] I.M. K, Teploobmen mezhdu tverdym telom I geliem-II, Z. Eksp. Teor. Fiz. 22 (1952) 687–704.
[62] E.T. Swartz, R.O. Pohl, Thermal boundary resistance, Rev. Mod. Phys. 61 (1989) 605–668.
[63] A. Liao, R. Alizadegan, Z.-Y. Ong, S. Dutta, F. Xiong, K.J. Hsia, E. Pop, Thermal dissipation and variability in electrical breakdown of carbon nanotube devices, Phys. Rev. B 82 (2010) 205406.
[64] J.C. Duda, J.L. Smoyer, P.M. Norris, P.E. Hopkins, Extension of the diffuse mismatch model for thermal boundary conductance between isotropic and anisotropic materials, Appl. Phys. Lett. 95 (2009), 031912.
[65] P. Hopkins, P. Norris, R. Stevens, Influence of inelastic scattering at metal-dielectric interfaces, J. Heat Tran. 130 (2008), 022401.
[66] T. Feng, Y. Zhong, J. Shi, X. Ruan, Unexpected high inelastic phonon transport across solid-solid interface: modal nonequilibrium molecular dynamics simulations and Landauer analysis, Phys. Rev. B 99 (2019), 045301.
[67] P. Norris, J. Smoyer, J. Duda, P. Hopkins, Prediction and measurement of thermal transport across interfaces between isotropic solids and graphitic materials, J. Heat Tran. 134 (2012), 020910.
[68] P.E. Hopkins, Multiple phonon processes contributing to inelastic scattering during thermal boundary conductance at solid interfaces, J. Appl. Phys. 106 (2009), 013528.
[69] Y. Zhang, D. Ma, Y. Zang, X. Wang, N. Yang, A modified theoretical model to accurately account for interfacial roughness in predicting the interfacial thermal conductance, Front. Energy Res. 6 (2018) 48.
[70] J. Lombard, F. Detcheverry, S. Merabia, Influence of the electron–phonon interfacial conductance on the thermal transport at metal/dielectric interfaces, J. Phys.:Condes. Matter 27 (2014), 015007.
[71] F. Gao, J. Qu, M. Yao, Interfacial thermal resistance between metallic carbon nanotube and Cu substrate, J. Appl. Phys. 110 (2011) 124314.
[72] D. Singh, J.Y. Murthy, T.S. Fisher, Mechanism of thermal conductivity reduction in few-layer graphene, J. Appl. Phys. 110 (2011), 044317.
[73] W.-R. Zhong, M.-P. Zhang, B.-Q. Ai, D.-Q. Zheng, Chirality and thickness-dependent thermal conductivity of few-layer graphene: a molecular dynamics study, Appl. Phys. Lett. 98 (2011) 113107.
[74] H.-Y. Cao, Z.-X. Guo, H. Xiang, X.-G. Gong, Layer and size dependence of

thermal conductivity in multilayer graphene nanoribbons, Phys. Lett. A 376 (2012) 525–528.
[75] Z.-X. Guo, D. Zhang, X.-G. Gong, Manipulating thermal conductivity through substrate coupling, Phys. Rev. B 84 (2011), 075470.
[76] M.M. Sadeghi, I. Jo, L. Shi, Phonon-interface scattering in multilayer graphene on an amorphous support, Proc. Natl. Acad. Sci. Unit. States Am. 110 (2013) 16321–16326.
[77] Z.-Y. Ong, E. Pop, Effect of substrate modes on thermal transport in supported graphene, Phys. Rev. B 84 (2011), 075471.
[78] W.-R. Zhong, Different thermal conductance of the inter- and intrachain interactions in a double-stranded molecular structure, Phys. Rev. E 81 (2010), 061131.
[79] Z. Guo, D. Zhang, Y. Zhai, X.-G. Gong, The intriguing thermal conductivity of ice nanotubes, Nanotechnology 21 (2010) 285706.
[80] G.L. Pollack, Kapitza resistance, Rev. Mod. Phys. 41 (1969) 48–81.
[81] H. Zhong, J.R. Lukes, Interfacial thermal resistance between carbon nanotubes: molecular dynamics simulations and analytical thermal modeling, Phys. Rev. B 74 (2006) 125403.
[82] M. Hu, P. Keblinski, J.-S. Wang, N. Raravikar, Interfacial thermal conductance between silicon and a vertical carbon nanotube, J. Appl. Phys. 104 (2008), 083503.
[83] B.A. Cola, J. Xu, T.S. Fisher, Contact mechanics and thermal conductance of carbon nanotube array interfaces, Int. J. Heat Mass Tran. 52 (2009) 3490–3503.
[84] B. Liu, J.A. Baimova, C.D. Reddy, S.V. Dmitriev, W.K. Law, X.Q. Feng, K. Zhou, Interface thermal conductance and rectification in hybrid graphene/silicene monolayer, Carbon 79 (2014) 236–244.
[85] K. Sääskilahti, J. Oksanen, J. Tulkki, S. Volz, Role of anharmonic phonon scattering in the spectrally decomposed thermal conductance at planar interfaces, Phys. Rev. B 90 (2014) 134312.
[86] L. Qiu, X. Wang, G. Su, D. Tang, X. Zheng, J. Zhu, Z. Wang, P.M. Norris, P.D. Bradford, Y. Zhu, Remarkably enhanced thermal transport based on a flexible horizontally-aligned carbon nanotube array film, Sci. Rep. 6 (2016) 21014.
[87] L. Qiu, K. Scheider, S.A. Radwan, L.S. Larkin, C.B. Saltonstall, Y. Feng, X. Zhang, P.M. Norris, Thermal transport barrier in carbon nanotube array nano-thermal interface materials, Carbon 120 (2017) 128–136.
[88] Y. Chen, Y. Zhang, K. Cai, J. Jiang, J.-C. Zheng, J. Zhao, N. Wei, Interfacial thermal conductance in graphene/black phosphorus heterogeneous structures, Carbon 117 (2017) 399–410.
[89] Y. Li, A. Wei, D. Datta, Thermal characteristics of graphene nanoribbons endorsed by surface functionalization, Carbon 113 (2017) 274–282.
[90] Y. Feng, J. Zhu, D. Tang, Dependence of carbon nanotube array-silicon interface thermal conductance on array arrangement and filling fraction, Appl. Therm. Eng. 145 (2018) 667–673.
[91] Z.-Y. Ong, E. Pop, Molecular dynamics simulation of thermal boundary conductance between carbon nanotubes and SiO_2, Phys. Rev. B 81 (2010) 155408.
[92] Y. Hong, L. Li, X.C. Zeng, J. Zhang, Tuning thermal contact conductance at graphene–copper interface via surface nanoengineering, Nanoscale 7 (2015) 6286–6294.
[93] S. Chen, M. Yang, B. Liu, M. Xu, T. Zhang, B. Zhuang, D. Ding, X. Huai, H. Zhang, Enhanced thermal conductance at the graphene–water interface based on functionalized alkane chains, RSC Adv. 9 (2019) 4563–4570.
[94] P.A. Greaney, J.C. Grossman, Nanomechanical energy transfer and resonance effects in single-walled carbon nanotubes, Phys. Rev. Lett. 98 (2007) 125503.
[95] R.S. Prasher, X.J. Hu, Y. Chalopin, N. Mingo, K. Lofgreen, S. Volz, F. Cleri, P. Keblinski, Turning carbon nanotubes from exceptional heat conductors into insulators, Phys. Rev. Lett. 102 (2009) 105901.
[96] Z. Xu, M.J. Buehler, Nanoengineering heat transfer performance at carbon nanotube interfaces, ACS Nano 3 (2009) 2767–2775.
[97] V. Varshney, J. Lee, D. Li, J.S. Brown, B.L. Farmer, A.A. Voevodin, A.K. Roy, Understanding thermal conductance across multi-wall carbon nanotube contacts: role of nanotube curvature, Carbon 114 (2017) 15–22.
[98] V. Varshney, J. Lee, J.S. Brown, B.L. Farmer, A.A. Voevodin, A.K. Roy, Effect of length, diameter, chirality, deformation, and strain on contact thermal conductance between single-wall carbon nanotubes, Front. Mater. 5 (2018) 17.
[99] Z. Ding, Q.-X. Pei, J.-W. Jiang, W. Huang, Y.-W. Zhang, Interfacial thermal conductance in graphene/MoS_2 heterostructures, Carbon 96 (2016) 888–896.
[100] B. Liu, J.A. Baimova, C.D. Reddy, A.W.-K. Law, S.V. Dmitriev, H. Wu, K. Zhou, Interfacial thermal conductance of a silicene/graphene bilayer heterostructure and the effect of hydrogenation, ACS Appl. Mater. Interfaces 6 (2014) 18180–18188.
[101] S. Namsani, J.K. Singh, Enhancement of thermal energy transport across the gold-graphene interface using nanoscale defects: a molecular dynamics study, J. Phys. Chem. C 122 (2018) 2113–2121.
[102] W. Zheng, B. Huang, H. Li, Y.K. Koh, Achieving huge thermal conductance of metallic nitride on graphene through enhanced elastic and inelastic phonon transmission, ACS Appl. Mater. Interfaces 10 (2018) 35487–35494.
[103] Y.K. Koh, A.S. Lyons, M.-H. Bae, B. Huang, V.E. Dorgan, D.G. Cahill, E. Pop, Role of remote interfacial phonon (RIP) scattering in heat transport across graphene/SiO_2 interfaces, Nano Lett. 16 (2016) 6014–6020.
[104] V. Perebeinos, S.V. Rotkin, A.G. Petrov, P. Avouris, The effects of substrate phonon mode scattering on transport in carbon nanotubes, Nano Lett. 9 (2009) 312–316.
[105] J.-H. Chen, C. Jang, S. Xiao, M. Ishigami, M.S. Fuhrer, Intrinsic and extrinsic performance limits of graphene devices on SiO_2, Nat. Nanotechnol. 3 (2008) 206–209.
[106] I. Meric, M.Y. Han, A.F. Young, B. Ozyilmaz, P. Kim, K.L. Shepard, Current saturation in zero-bandgap, top-gated graphene field-effect transistors, Nat. Nanotechnol. 3 (2008) 654–659.
[107] Y. Wang, Z. Song, Z. Xu, Characterizing phonon thermal conduction in polycrystalline graphene, J. Mater. Res. 29 (2014) 362–372.
[108] W. Zhao, Y. Wang, Z. Wu, W. Wang, K. Bi, Z. Liang, J. Yang, Y. Chen, Z. Xu, Z. Ni, Defect-engineered heat transport in graphene: a route to high efficient thermal rectification, Sci. Rep. 5 (2015) 11962.
[109] Y. Wang, Z. Qin, M.J. Buehler, Z. Xu, Intercalated water layers promote thermal dissipation at bio-nano interfaces, Nat. Commun. 7 (2016) 12854.
[110] Y. Wang, Z. Xu, Water intercalation for seamless, electrically insulating, and thermally transparent interfaces, ACS Appl. Mater. Interfaces 8 (2016) 1970–1976.
[111] H.Y. Zhang, X. Gu, X.H. Zhang, X. Ye, X.G. Gong, Structures and properties of Ni nanowires, Phys. Lett. A 331 (2004) 332–336.
[112] L. Yang, M.Y. Chou, Lattice vibrational modes and their frequency shifts in semiconductor nanowires, Nano Lett. 11 (2011) 2618–2621.
[113] G.-Y. Huang, Y.-L. Kang, Acoustic vibrations of a circular nanowire by considering the effect of surface, J. Appl. Phys. 110 (2011), 023526.
[114] L. Saviot, Vibrations of single-crystal gold nanorods and nanowires, Phys. Rev. B 97 (2018) 155420.
[115] L. Qiu, H. Zou, X. Wang, Y. Feng, X. Zhang, J. Zhao, X. Zhang, Q. Li, Enhancing the interfacial interaction of carbon nanotubes fibers by Au nanoparticles with improved performance of the electrical and thermal conductivity, Carbon 141 (2019) 497–505.
[116] Q. Lin, H. Zou, N. Zhu, Y. Feng, X. Zhang, X. Zhang, Iodine nanoparticle-enhancing electrical and thermal transport for carbon nanotube fibers, Appl. Therm. Eng. 141 (2018) 913–920.
[117] L. Liu, W. Ma, Z. Zhang, Macroscopic carbon nanotube Assemblies: preparation, properties, and potential applications, Small 7 (2011) 1504–1520.
[118] Z. Li, Z. Liu, H. Sun, C. Gao, Superstructured assembly of nanocarbons: fullerenes, nanotubes, and graphene, Chem. Rev. 115 (2015) 7046–7117.
[119] H. Cheng, C. Hu, Y. Zhao, L. Qu, Graphene fiber: a new material platform for unique applications, NPG Asia Mater. 6 (2014) e113.
[120] J. Di, X. Wang, Y. Xing, Y. Zhang, X. Zhang, W. Lu, Q. Li, Y.T. Zhu, Dry-processable carbon nanotubes for functional devices and composites, Small 10 (2014) 4606–4625.
[121] Z. Xu, C. Gao, Graphene fiber: a new trend in carbon fibers, Mater. Today 18 (2015) 480–492.
[122] J. Di, X. Zhang, Z. Yong, Y. Zhang, D. Li, R. Li, Q. Li, Carbon-nanotube fibers for wearable devices and smart textiles, Adv. Mater. 28 (2016) 10529–10538.
[123] X. Zhang, W. Lu, G. Zhou, Q. Li, Understanding the mechanical and conductive properties of carbon nanotube fibers for smart electronics, Adv. Mater. 32 (2020) 1902028.
[124] M.B. Bryning, D.E. Milkie, M.F. Islam, L.A. Hough, J.M. Kikkawa, A.G. Yodh, Carbon nanotube Aerogels, Adv. Mater. 19 (2007) 661–664.
[125] J. Feng, J. Feng, C. Zhang, Thermal conductivity of low density carbon aerogels, J. Porous Mater. 19 (2012) 551–556.
[126] X. Lu, M.C. Arduini-Schuster, J. Kuhn, O. Nilsson, J. Fricke, R.W. Pekala, Thermal conductivity of monolithic organic aerogels, Science 255 (1992) 971–972.
[127] X. Lu, O. Nilsson, J. Fricke, R.W. Pekala, Thermal and electrical conductivity of monolithic carbon aerogels, J. Appl. Phys. 73 (1993) 581–584.
[128] Y. Xie, S. Xu, Z. Xu, H. Wu, C. Deng, X. Wang, Interface-mediated extremely low thermal conductivity of graphene aerogel, Carbon 98 (2016) 381–390.
[129] Y. Cheng, S. Zhou, P. Hu, G. Zhao, Y. Li, X. Zhang, W. Han, Enhanced mechanical, thermal, and electric properties of graphene aerogels via supercritical ethanol drying and high-temperature thermal reduction, Sci. Rep. 7 (2017) 1439.
[130] Z. Fan, D.Z.Y. Tng, C.X.T. Lim, P. Liu, S.T. Nguyen, P. Xiao, A. Marconnet, C.Y.H. Lim, H.M. Duong, Thermal and electrical properties of graphene/carbon nanotube aerogels, Colloids Surf., A 445 (2014) 48–53.
[131] M.T. Pettes, H. Ji, R.S. Ruoff, L. Shi, Thermal transport in three-Dimensional foam architectures of few-layer graphene and ultrathin graphite, Nano Lett. 12 (2012) 2959–2964.
[132] M. Zhou, T. Lin, F. Huang, Y. Zhong, Z. Wang, Y. Tang, H. Bi, D. Wan, J. Lin, Highly conductive porous graphene/ceramic composites for heat transfer and thermal energy storage, Adv. Funct. Mater. 23 (2013) 2263–2269.
[133] Q. Liang, X. Yao, W. Wang, Y. Liu, C.P. Wong, A three-dimensional vertically aligned functionalized multilayer graphene architecture: an approach for graphene-based thermal interfacial materials, ACS Nano 5 (2011) 2392–2401.
[134] M. Wang, H. Chen, W. Lin, Z. Li, Q. Li, M. Chen, F. Meng, Y. Xing, Y. Yao, C.-p. Wong, Q. Li, Crack-free and scalable transfer of carbon nanotube Arrays into flexible and highly thermal conductive composite film, ACS Appl. Mater. Interfaces 6 (2014) 539–544.
[135] I. Ivanov, A. Puretzky, G. Eres, H. Wang, Z. Pan, H. Cui, R. Jin, J. Howe, D.B. Geohegan, Fast and highly anisotropic thermal transport through vertically aligned carbon nanotube arrays, Appl. Phys. Lett. 89 (2006) 223110.

[136] E.C. Samson, S.V. Machiroutu, J.-Y. Chang, I. Santos, J. Hermerding, A. Dani, R. Prasher, D.W. Song, Interface material selection and a thermal management technique in second-generation platforms built on intel centrino mobile technology, Intel Technol. J. 9 (2005) 75–86.
[137] Y. Xu, Y. Zhang, E. Suhir, X. Wang, Thermal properties of carbon nanotube array used for integrated circuit cooling, J. Appl. Phys. 100 (2006), 074302.
[138] S. Shaikh, L. Li, K. Lafdi, J. Huie, Thermal conductivity of an aligned carbon nanotube array, Carbon 45 (2007) 2608–2613.
[139] M.B. Jakubinek, M.A. White, G. Li, C. Jayasinghe, W. Cho, M.J. Schulz, V. Shanov, Thermal and electrical conductivity of tall, vertically aligned carbon nanotube arrays, Carbon 48 (2010) 3947–3952.
[140] M. Akoshima, K. Hata, D.N. Futaba, K. Mizuno, T. Baba, M. Yumura, Thermal diffusivity of single-walled carbon nanotube forest measured by laser flash method, Jpn. J. Appl. Phys. 48 (2009), 05EC07.
[141] A.M. Marconnet, N. Yamamoto, M.A. Panzer, B.L. Wardle, K.E. Goodson, Thermal conduction in aligned carbon nanotube-polymer nanocomposites with high packing density, ACS Nano 5 (2011) 4818–4825.
[142] H. Sugime, S. Esconjauregui, J. Yang, L. D'Arsié, R.A. Oliver, S. Bhardwaj, C. Cepek, J. Robertson, Low temperature growth of ultra-high mass density carbon nanotube forests on conductive supports, Appl. Phys. Lett. 103 (2013), 073116.
[143] M.A. Panzer, G. Zhang, D. Mann, X. Hu, E. Pop, H. Dai, K.E. Goodson, Thermal properties of metal-coated vertically aligned single-wall nanotube Arrays, J. Heat Tran. 130 (2008), 052401.
[144] J. Hone, M.C. Llaguno, N.M. Nemes, A.T. Johnson, J.E. Fischer, D.A. Walters, M.J. Casavant, J. Schmidt, R.E. Smalley, Electrical and thermal transport properties of magnetically aligned single wall carbon nanotube films, Appl. Phys. Lett. 77 (2000) 666–668.
[145] P. Gonnet, Z. Liang, E.S. Choi, R.S. Kadambala, C. Zhang, J.S. Brooks, B. Wang, L. Kramer, Thermal conductivity of magnetically aligned carbon nanotube buckypapers and nanocomposites, Curr. Appl. Phys. 6 (2006) 119–122.
[146] D. Wang, P. Song, C. Liu, W. Wu, S. Fan, Highly oriented carbon nanotube papers made of aligned carbon nanotubes, Nanotechnology 19 (2008), 075609.
[147] K. Yang, J. He, P. Puneet, Z. Su, M.J. Skove, J. Gaillard, T.M. Tritt, A.M. Rao, Tuning electrical and thermal connectivity in multiwalled carbon nanotube buckypaper, J. Phys. Condens. Matter 22 (2010) 334215.
[148] Y. Yue, X. Huang, X. Wang, Thermal transport in multiwall carbon nanotube buckypapers, Phys. Lett. A 374 (2010) 4144–4151.
[149] H. Chen, M. Chen, J. Di, G. Xu, H. Li, Q. Li, Architecting three-dimensional networks in carbon nanotube buckypapers for thermal interface materials, J. Phys. Chem. C 116 (2012) 3903–3909.
[150] Y. Xing, X. Zhang, H. Chen, M. Chen, Q. Li, Enhancing buckypaper conductivity through co-deposition with copper nanowires, Carbon 61 (2013) 501–506.
[151] S. Sahoo, V.R. Chitturi, R. Agarwal, J.-W. Jiang, R.S. Katiyar, Thermal conductivity of freestanding single wall carbon nanotube sheet by Raman spectroscopy, ACS Appl. Mater. Interfaces 6 (2014) 19958–19965.
[152] A. Duzynska, A. Taube, K.P. Korona, J. Judek, M. Zdrojek, Temperature-dependent thermal properties of single-walled carbon nanotube thin films, Appl. Phys. Lett. 106 (2015) 183108.
[153] X. Zhang, W. Tan, F. Smail, M. De Volder, N. Fleck, A. Boies, High-fidelity characterization on anisotropic thermal conductivity of carbon nanotube sheets and on their effects of thermal enhancement of nanocomposites, Nanotechnology 29 (2018) 365708.
[154] Y. Zhao, Y. Yan, A. Kumar, H. Wang, W.D. Porter, S. Priya, Thermal conductivity of self-assembled nano-structured ZnO bulk ceramics, J. Appl. Phys. 112 (2012), 034313.
[155] H.E. Misak, J.L. Rutledge, E.D. Swenson, S. Mall, Thermal transport properties of dry spun carbon nanotube sheets, J. Nanomater. 2016 (2016) 9174085.
[156] B.W. Smith, Z. Benes, D.E. Luzzi, J.E. Fischer, D.A. Walters, M.J. Casavant, J. Schmidt, R.E. Smalley, Structural anisotropy of magnetically aligned single wall carbon nanotube films, Appl. Phys. Lett. 77 (2000) 663–665.
[157] L. Zhang, G. Zhang, C. Liu, S. Fan, High-density carbon nanotube buckypapers with superior transport and mechanical properties, Nano Lett. 12 (2012) 4848–4852.
[158] J. Ding, H. Zhao, Q. Wang, H. Dou, H. Chen, H. Yu, An ultrahigh thermal conductive graphene flexible paper, Nanoscale 9 (2017) 16871–16878.
[159] Y. Xie, P. Yuan, T. Wang, N. Hashemi, X. Wang, Switch on the high thermal conductivity of graphene paper, Nanoscale 8 (2016) 17581–17597.
[160] M.B. Jakubinek, M.B. Johnson, M.A. White, C. Jayasinghe, G. Li, W. Cho, M.J. Schulz, V. Shanov, Thermal and electrical conductivity of array-spun multi-walled carbon nanotube yarns, Carbon 50 (2012) 244–248.
[161] L.M. Ericson, H. Fan, H. Peng, V.A. Davis, W. Zhou, J. Sulpizio, Y. Wang, R. Booker, J. Vavro, C. Guthy, A.N.G. Parra-Vasquez, M.J. Kim, S. Ramesh, R.K. Saini, C. Kittrell, G. Lavin, H. Schmidt, W.W. Adams, W.E. Billups, M. Pasquali, W.-F. Hwang, R.H. Hauge, J.E. Fischer, R.E. Smalley, Macroscopic, neat, single-walled carbon nanotube fibers, Science 305 (2004) 1447–1450.
[162] N. Behabtu, C.C. Young, D.E. Tsentalovich, O. Kleinerman, X. Wang, A.W.K. Ma, E.A. Bengio, R.F. ter Waarbeek, J.J. de Jong, R.E. Hoogerwerf, S.B. Fairchild, J.B. Ferguson, B. Maruyama, J. Kono, Y. Talmon, Y. Cohen, M.J. Otto, M. Pasquali, Strong, light, multifunctional fibers of carbon nanotubes with ultrahigh conductivity, Science 339 (2013) 182–186.
[163] G. Xin, T. Yao, H. Sun, S.M. Scott, D. Shao, G. Wang, J. Lian, Highly thermally conductive and mechanically strong graphene fibers, Science 349 (2015) 1083–1087.
[164] J. Zhu, Thermal property of carbon nanotube fibers from chemical vapor deposition synthesis, in: G. Zhang, M. Lee (Eds.), Proceedings of the 2015 International Conference on Materials, Environmental and Biological Engineering, Volume 10 of *AER-Advances In Engineering Research*, Atlantis Press, Paris, 2015, pp. 919–922.
[165] L. Qiu, X. Wang, D. Tang, X. Zheng, P.M. Norris, D. Wen, J. Zhao, X. Zhang, Q. Li, Functionalization and densification of inter-bundle interfaces for improvement in electrical and thermal transport of carbon nanotube fibers, Carbon 105 (2016) 248–259.
[166] P. Liu, Z. Fan, A. Mikhalchan, T.Q. Tran, D. Jewell, H.M. Duong, A.M. Marconnet, Continuous carbon nanotube-based fibers and films for applications requiring enhanced heat dissipation, ACS Appl. Mater. Interfaces 8 (2016) 17461–17471.
[167] T.S. Gspann, S.M. Juckes, J.F. Niven, M.B. Johnson, J.A. Elliott, M.A. White, A.H. Windle, High thermal conductivities of carbon nanotube films and micro-fibres and their dependence on morphology, Carbon 114 (2017) 160–168.
[168] Y. Li, X. Li, M.M. Alam, D. Yu, J. Miao, M. Cao, P. Chen, R. Xia, B. Wu, J. Qian, Incorporating Ag nanowires into graphene nanosheets for enhanced thermal conductivity: implications for thermal management, ACS Appl. Nano Mater. 3 (2020) 6061–6070.
[169] L. Qiu, P. Guo, X. Yang, Y. Ouyang, Y. Feng, X. Zhang, J. Zhao, X. Zhang, Q. Li, Electro curing of oriented bismaleimide between aligned carbon nanotubes for high mechanical and thermal performances, Carbon 145 (2019) 650–657.
[170] L. Qiu, N. Zhu, Y. Feng, X. Zhang, X. Wang, Interfacial thermal transport properties of polyurethane/carbon nanotube hybrid composites, Int. J. Heat Mass Tran. 152 (2020) 119565.
[171] G. Yang, H. Yi, Y. Yao, C. Li, Z. Li, Thermally conductive graphene films for heat dissipation, ACS Appl. Nano Mater. 3 (2020) 2149–2155.
[172] L. Qiu, P. Guo, Q. Kong, C.W. Tan, K. Liang, J. Wei, J.N. Tey, Y. Feng, X. Zhang, B.K. Tay, Coating-boosted interfacial thermal transport for carbon nanotube array nano-thermal interface materials, Carbon 145 (2019) 725–733.
[173] A.M. Marconnet, M.A. Panzer, K.E. Goodson, Thermal conduction phenomena in carbon nanotubes and related nanostructured materials, Rev. Mod. Phys. 85 (2013) 1295–1326.
[174] Y. Chalopin, S. Volz, N. Mingo, Upper bound to the thermal conductivity of carbon nanotube pellets, J. Appl. Phys. 105 (2009), 084301.
[175] A.N. Volkov, L.V. Zhigilei, Scaling laws and mesoscopic modeling of thermal conductivity in carbon nanotube materials, Phys. Rev. Lett. 104 (2010) 215902.
[176] A.N. Volkov, L.V. Zhigilei, Heat conduction in carbon nanotube materials: strong effect of intrinsic thermal conductivity of carbon nanotubes, Appl. Phys. Lett. 101 (2012), 043113.
[177] A.N. Volkov, R.N. Salaway, L.V. Zhigilei, Atomistic simulations, mesoscopic modeling, and theoretical analysis of thermal conductivity of bundles composed of carbon nanotubes, J. Appl. Phys. 114 (2013) 104301.
[178] J.N. Fox, N.W. Gaggini, R. Wangsani, Measurement of the thermal conductivity of liquids using a transient hot wire technique, Am. J. Phys. 55 (1987) 272–274.
[179] S. Harish, D. Orejon, Y. Takata, M. Kohno, Enhanced thermal conductivity of phase change nanocomposite in solid and liquid state with various carbon nano inclusions, Appl. Therm. Eng. 114 (2017) 1240–1246.
[180] J. Chen, X. Gui, Z. Wang, Z. Li, R. Xiang, K. Wang, D. Wu, X. Xia, Y. Zhou, Q. Wang, Z. Tang, L. Chen, Superlow thermal conductivity 3D carbon nanotube network for thermoelectric applications, ACS Appl. Mater. Interfaces 4 (2012) 81–86.
[181] X. Chen, H. Gao, M. Yang, W. Dong, X. Huang, A. Li, C. Dong, G. Wang, Highly graphitized 3D network carbon for shape-stabilized composite PCMs with superior thermal energy harvesting, Nano Energy 49 (2018) 86–94.
[182] E.C. Cho, C.W. Changjian, Y. Hsiao, K.C. Lee, J. Huang, Three-dimensional carbon nanotube based polymer composites for thermal management, Compos. Part A 90 (2016) 678–686.
[183] W. Zaman, K. Li, S. Ikram, W. Li, D. Zhang, L. Guo, Morphology, thermal response and anti-ablation performance of 3D-four directional pitch-based carbon/carbon composites, Corrosion Sci. 61 (2012) 134–142.
[184] J. Pasieka, N. Hordy, S. Coulombe, P. Servio, Measuring the effect of multi-Wall carbon nanotubes on tetrahydrofuran-water hydrate front velocities using thermal imaging, Cryst. Growth Des. 13 (2013) 4017–4024.
[185] Q. Kong, L. Bodelot, B. Lebental, Y.D. Lim, L.L. Shiau, B. Gusarov, C.W. Tan, K. Liang, C. Lu, C.S. Tan, P. Coquet, B.K. Tay, Novel three-dimensional carbon nanotube networks as high performance thermal interface materials, Carbon 132 (2018) 359–369.
[186] J.D. Craddock, J.J. Burgess, S.E. Edrington, M.C. Weisenberger, Method for direct measurement of on-axis carbon fiber thermal diffusivity using the laser flash technique, J. Therm. Sci. Eng. Appl. 9 (2017), 014502.
[187] Q.-Y. Li, K. Xia, J. Zhang, Y. Zhang, Q. Li, K. Takahashi, X. Zhang, Measurement of specific heat and thermal conductivity of supported and suspended graphene by a comprehensive Raman optothermal method, Nanoscale 9 (2017) 10784–10793.
[188] T.L. Bougher, J.H. Taphouse, B.A. Cola, Characterization of carbon nanotube forest interfaces using time domain thermoreflectance, in: Proceedings of the ASME 2015 International Technical Conference and Exhibition on Packaging and Integration of Electronic and Photonic Microsystems, San Francisco, California, USA, 2015, pp. IPACK2015–48587, https://doi.org/

10.1115/IPACK2015-48587.
[189] E. Mayhew, V. Prakash, Thermal conductivity of high performance carbon nanotube yarn-like fibers, Appl. Phys. Lett. 115 (2014) 174306.
[190] Z. Wang, R. Xie, C.T. Bui, D. Liu, X. Ni, B. Li, J.T.L. Thong, Thermal transport in suspended and supported few-layer graphene, Nano Lett. 11 (2011) 113–118.
[191] L. Qiu, Y. Ouyang, Y. Feng, X. Zhang, Note: thermal conductivity measurement of individual porous polyimide fibers using a modified wire-shape 3ω method, Rev. Sci. Instrum. 89 (2018), 096112.
[192] T.R. Hart, R.L. Aggarwal, B. Lax, Temperature dependence of Raman scattering in silicon, Phys. Rev. B 1 (1970) 638–642.
[193] S. Sahoo, A.P.S. Gaur, M. Ahmadi, M.J.-F. Guinel, R.S. Katiyar, Temperature-dependent Raman studies and thermal conductivity of few-layer MoS_2, J. Phys. Chem. C 117 (2013) 9042–9047.
[194] S. Xu, A. Fan, H. Wang, X. Zhang, X. Wang, Raman-based nanoscale thermal transport characterization: a critical review, Int. J. Heat Mass Tran. 154 (2020) 119751.
[195] P. Yuan, R. Wang, H. Tan, T. Wang, X. Wang, Energy transport state resolved Raman for probing interface energy transport and hot carrier diffusion in few-layered MoS_2, ACS Photonics 4 (2017) 3115–3129.
[196] H. Zobeiri, R. Wang, T. Wang, H. Lin, C. Deng, X. Wang, Frequency-domain energy transport state-resolved Raman for measuring the thermal conductivity of suspended nm-thick $MoSe_2$, Int. J. Heat Mass Tran. 133 (2019) 1074–1085.
[197] Q. Li, X. Zhang, K. Takahashi, Variable-spot-size laser-flash Raman method to measure in-plane and interfacial thermal properties of 2D van der Waals heterostructures, Int. J. Heat Mass Tran. 125 (2018) 1230–1239.
[198] S. Xu, T. Wang, H. David, Y. Yue, X. Wang, Development of time-domain differential Raman for transient thermal probing of materials, Opt Express 23 (2015) 10040–10056.
[199] S. Ghosh, I. Calizo, D. Teweldebrhan, E.P. Pokatilov, D.L. Nika, A.A. Balandin, W. Bao, F. Miao, C.N. Lau, Extremely high thermal conductivity of graphene: prospects for thermal management applications in nanoelectronic circuits, Appl. Phys. Lett. 92 (2008) 151911.
[200] A.K. Vallabhaneni, D. Singh, H. Bao, J. Murthy, X. Ruan, Reliability of Raman measurements of thermal conductivity of single-layer graphene due to selective electron-phonon coupling: a first-principles study, Phys. Rev. B 93 (2016) 125432.
[201] D.J. Yang, Q. Zhang, G. Chen, S.F. Yoon, J. Ahn, S.G. Wang, Q. Zhou, Q. Wang, J.Q. Li, Thermal conductivity of multiwalled carbon nanotubes, Phys. Rev. B 66 (2002) 165440.
[202] K. Ujihara, Reflectivity of metals at high temperatures, IEEE J. Quant. Electron. 8 (1972) 567–568.
[203] J. Zhu, X. Wu, D.M. Lattery, W. Zheng, X. Wang, The ultrafast laser pump-probe technique for thermal characterization of materials with micro/nanostructures, Nanoscale Microscale Thermophys. Eng. 21 (2017) 177–198.
[204] A.J. Schmidt, K.C. Collins, A.J. Minnich, G. Chen, Thermal conductance and phonon transmissivity of metal–graphite interfaces, J. Appl. Phys. 107 (2010) 104907.
[205] Y.K. Koh, M.-H. Bae, D.G. Cahill, E. Pop, Heat conduction across monolayer and few-layer graphenes, Nano Lett. 10 (2010) 4363–4368.
[206] P. Jiang, X. Qian, R. Yang, Time-domain thermoreflectance (TDTR) measurements of anisotropic thermal conductivity using a variable spot size approach, Rev. Sci. Instrum. 88 (2017), 074901.
[207] P. Kim, L. Shi, A. Majumdar, P.L. McEuen, Thermal transport measurements of individual multiwalled nanotubes, Phys. Rev. Lett. 87 (2001) 215502.
[208] M. Fujii, X. Zhang, H. Xie, H. Ago, K. Takahashi, T. Ikuta, H. Abe, T. Shimizu, Measuring the thermal conductivity of a single carbon nanotube, Phys. Rev. Lett. 95 (2005), 065502.
[209] Q. Li, C. Liu, X. Wang, S. Fan, Measuring the thermal conductivity of individual carbon nanotubes by the Raman shift method, Nanotechnology 20 (2009) 145702.
[210] Q. Li, C. Liu, S. Fan, Thermal boundary resistances of carbon nanotubes in contact with metals and polymers, Nano Lett. 9 (2009) 3805–3809.
[211] I.-K. Hsu, M.T. Pettes, A. Bushmaker, M. Aykol, L. Shi, S.B. Cronin, Optical absorption and thermal transport of individual suspended carbon nanotube bundles, Nano Lett. 9 (2009) 590–594.
[212] J.L. Wang, M. Gu, X. Zhang, Y. Song, Thermal conductivity measurement of an individual fibre using a T type probe method, J. Phys. D Appl. Phys. 42 (2009) 105502.
[213] L. Shi, D. Li, C. Yu, W. Jang, D. Kim, Z. Yao, P. Kim, A. Majumdar, Measuring thermal and thermoelectric properties of one-dimensional nanostructures using a microfabricated device, J. Heat Tran. 125 (2003) 881–888.
[214] Y. Fu, J. Hansson, Y. Liu, S. Chen, A. Zehri, M.K. Samani, N. Wang, Y. Ni, Y. Zhang, Z. Zhang, Q. Wang, M. Li, H. Lu, M. Sledzinska, C.M.S. Torres, S. Volz, A.A. Balandin, X. Xu, J. Liu, Graphene related materials for thermal management, 2D Mater. 7 (2019), 012001.
[215] J. Liu, H. Liu, Y. Hu, X. Zhang, Differential laser flash Raman spectroscopy method for non-contact characterization of thermal transport properties of individual nanowires, Int. J. Heat Mass Tran. 135 (2019) 511–516.
[216] C. Li, S. Xu, Y. Yue, B. Yang, X. Wang, Thermal characterization of carbon nanotube fiber by time-domain differential Raman, Carbon 103 (2016) 101–108.
[217] Q.-Y. Li, K. Katakami, T. Ikuta, M. Kohno, X. Zhang, K. Takahashi, Thermal characterization of carbon nanotube fiber by time-domain differential Raman, Carbon 141 (2019) 92–98.
[218] T.-Y. Choi, D. Poulikakos, J. Tharian, U. Sennhauser, Measurement of the thermal conductivity of individual carbon nanotubes by the four-point three-ω method, Nano Lett. 6 (2006) 1589–1593.
[219] Z.L. Wang, D.W. Tang, X.B. Li, X.H. Zheng, W.G. Zhang, L.X. Zheng, Y.T. Zhu, A.Z. Jin, H.F. Yang, C.Z. Gu, Length-dependent thermal conductivity of an individual single-wall carbon nanotube, Appl. Phys. Lett. 91 (2007) 123119.
[220] R.N. Salaway, L.V. Zhigilei, Molecular dynamics simulations of thermal conductivity of carbon nanotubes: resolving the effects of computational parameters, Int. J. Heat Mass Tran. 70 (2014) 954–964.
[221] W. Yi, L. Lu, D. Zhang, Z. Pan, S. Xie, Linear specific heat of carbon nanotubes, Phys. Rev. B 59 (1999) R9015–R9018.
[222] X.J. Hu, A.A. Padilla, J. Xu, T.S. Fisher, K.E. Goodson, 3-Omega measurements of vertically oriented carbon nanotubes on silicon, J. Heat Trans-T ASME 128 (2006) 1109–1113.
[223] A.E. Aliev, M.H. Lima, E.M. Silverman, R.H. Baughman, Thermal conductivity of multi-walled carbon nanotube sheets: radiation losses and quenching of phonon modes, Nanotechnology 21 (2010), 035709.
[224] T. Tong, M. A, Reexamining the 3-omega technique for thin film thermal characterization, Rev. Sci. Instrum. 77 (2006) 104902.
[225] S. Ahmed, R. Liske, T. Wunderer, M. Leonhardt, R. Ziervogel, C. Fansler, T.A. Grotjohn, J. Asmussen, T. Schuelke, Xtending the 3ω-method to the MHz range for thermal conductivity measurements of diamond thin films, Diam. Relat. Mater. 15 (2006) 389–393.
[226] D.G. Cahill, Thermal conductivity measurement from 30 to 750 K: the 3ωmethod, Rev. Sci. Instrum. 61 (1990) 802–808.
[227] N.O. Birge, P.K. Dixon, N. Menon, Specific heat spectroscopy: origins, status and applications of the 3ωmethod, Thermochim. Acta 304–305 (1997) 51–66.
[228] L. Qiu, X. Zheng, J. Zhu, D. Tang, S.Y. Yang, A.J. Hu, L. Wang, S. Li, Thermal transport in high-strength polymethacrylimide (PMI) foam insulations, Int. J. Thermophys. 36 (2015) 2523–2534.
[229] I. Moon, Y. Jeong, S. Kwun, The 3ωtechnique for measuring dynamic specific heat and thermal conductivity of a liquid or solid, Rev. Sci. Instrum. 67 (1996) 29–35.
[230] R.C. Sun, J. Kim, D. Kim, 3omega method to measure thermal properties of electrically conducting small-volume liquid, Rev. Sci. Instrum. 78 (2007) 45.
[231] L. Qiu, X. Zheng, G. Su, D. Tang, Design and application of a freestanding sensor based on 3ωtechnique for thermal-conductivity measurement of solids, liquids, and nanopowders, Int. J. Thermophys. 34 (2013) 2261–2275.
[232] X. Zheng, L. Qiu, G. Su, D. Tang, Y. Liao, Y. Chen, Thermal conductivity and thermal diffusivity of SiO_2 nanopowder, J. Nanopart. Res. 13 (2011) 6887–6893.